Measurement report: Molecular composition, optical properties, and radiative effects of water-soluble organic carbon in snowpack samples from Northern Xinjiang, China

Yue Zhou,[1,2] Christopher P. West,[2] Anusha P. S. Hettiyadura,[2] Xiaoying Niu,[1] Hui Wen,[1] Jiecan Cui,[1] Tenglong Shi,[1] Wei Pu,[1] Xin Wang,[1,4]* Alexander Laskin[2,3]*

[1] *Key Laboratory for Semi-Arid Climate Change of the Ministry of Education, College of Atmospheric Sciences, Lanzhou University, Lanzhou 730000, China*

[2] *Department of Chemistry,* [3] *Department of Earth Atmospheric and Planetary Sciences, Purdue University, West Lafayette, Indiana 47906, United States*

[4] *Institute of Surface-Earth System Science, Tianjin University, Tianjin 300072, China*

Correspondence to: Alexander Laskin (alaskin@purdue.edu) and Xin Wang (wxin@lzu.edu.cn)

Abstract. Water-soluble organic carbon (WSOC) in the cryosphere has important

impact on the biogeochemistry cycling and snow/ice surface energy balance through

changes in the surface albedo. This work reports on chemical characterization of WSOC

in 28 representative snowpack samples collected across regional area of northern

Xinjiang, northwestern China. We employed multi-modal analytical chemistry

techniques to investigate both bulk and molecular-level composition of WSOC and its

optical properties, informing the follow-up radiative forcing (*RF*) modeling estimates.

Based on the geographic differences and proximity of emission sources, the snowpack

collection sites were grouped as urban/industrial (U), rural/remote (R), and soil-

influenced (S) sites, for which average WSOC total mass loadings were measured as

1968 ± 953 ng g^{-1} (U), 885 ± 328 ng g^{-1} (R), and 2082 ± 1438 ng g^{-1} (S), respectively. The

S sites showed the higher mass absorption coefficients at 365 nm (MAC_{365}) of

0.94 ± 0.31 m^2 g^{-1} compared to those of U and R sites (0.39 ± 0.11 m^2 g^{-1} and 0.38 ± 0.12

m^2 g^{-1}, respectively). Bulk composition of WSOC in the snowpack samples and its basic

source apportionment was inferred from the Excitation-Emission Matrices and the

Parallel Factor analysis featuring relative contributions of two humic-like (HULIS-1

and HULIS-2) and one protein-like (PRLIS) components with ratios specific to each of

the S, U, and R sites. Additionally, a sample from site 120 showed unique pollutant

concentrations and spectroscopic features remarkably different from all other U, R, and

S samples. Molecular-level characterization of WSOC using high-resolution mass

spectrometry (HRMS) provided further insights into chemical differences among four

types of samples (U, R, S, and 120). Specifically, much more reduced S-containing

52   species with high degree of unsaturation and aromaticity were uniquely identified in U

53   samples, suggesting an anthropogenic source. Aliphatic/proteins-like species showed

54   highest contribution in R samples, indicating their biogenic origin. The WSOC

55   components from S samples showed high oxygenation and saturation levels. A few of

56   unique CHON and CHONS compounds with high unsaturation degree and molecular

57   weight were detected in the 120 sample, which might be anthraquinone derivatives from

58   plant debris. Modeling of the WSOC-induced RF values showed warming effects of

59   0.04 to 0.59 W m^{-2} among different groups of sites, which contribute up to 16% of that

60   caused by BC, demonstrating the important influences of WSOC on the snow energy

61   budget.

1 Introduction

As the largest component of the terrestrial cryosphere (Brutel-Vuilmet et al., 2013), snow covers up to 40% of Earth's land seasonally (Hall et al., 1995). Snowfall is a crucial fresh water, nutrient, and carbon source for land ecosystems (Jones, 1999;Mladenov et al., 2012), especially for barren regions such as the northwestern China (Xu et al., 2010). Chemical deposits in the snowpack are highly photochemically and biologically active, which in turn influence biogeochemical cycles and the atmospheric environment (Grannas et al., 2007;Liu et al., 2009). With respect to the climate effects, snow/ice surface has the highest albedo, which makes it the highest light reflecting surface on Earth and a key factor influencing the Earth's radiative balance. The deposition of light-absorbing particles (LAP), primarily black carbon (BC), organic carbon (OC), mineral dust (MD), and microbes, on snow reduces the snow albedo significantly and increases the absorption of solar radiation (Hadley and Kirchstetter, 2012;Skiles et al., 2018). Consequently, deposits of LAP accelerate snow melting (Hansen and Nazarenko, 2004) and affect the snow photochemistry (Zatko et al., 2013), further influencing the regional and global climate (Bond et al., 2013;Flanner et al., 2007;Jacobson, 2004). The albedo reduction and radiative forcing (RF) due to the BC and MD deposits in snow has been a subject of many field studies (Doherty et al., 2010;Huang et al., 2011;Pu et al., 2017;Shi et al., 2020;Wang et al., 2013, 2017b;Zhang et al., 2018b), remote sensing estimates (Painter et al., 2010;Pu et al., 2019), and climate models (He et al., 2014;Qian et al., 2014;Zhao et al., 2014). Darkening of snow by biological organisms, like snow algae common in high-altitude and high-latitude

85 snowpack, has also been investigated (Cook et al., 2017a, b;Ganey et al., 2017;Lutz et

86 al., 2014). However, yet little is known about the chemical compositions, optical

87 properties, and radiative effects of OC compounds in snow, which result from both

88 deposition of organic aerosol from natural and anthropogenic sources as well as

89 deposits of the wind-blown soil organic matter (Pu et al., 2017;Wang et al., 2013).

90 Water-soluble OC (WSOC) contributes to a large portion (10-80%) of organic

91 aerosol (Kirillova et al., 2014;Zhang et al., 2018a) and it is also widely distributed in

92 the cryosphere. The polar ice sheets and mountain glaciers store large amount of organic

93 carbon, which provide approximately 1.04 ± 0.18 TgC yr^{-1} of WSOC exported into

94 proglacial aquatic environments (Hood et al., 2015), with a substantial part of it is

95 highly bioavailable (Singer et al., 2012;Zhou et al., 2019c). WSOC components that

96 absorb solar radiation at ultraviolet to visible (UV-Vis) wavelengths are collectively

97 termed as "brown carbon (BrC)" (Andreae and Gelencser, 2006), and have become the

98 subject of many aerosol studies (Laskin et al., 2015). The optical properties of WSOC

99 in snow started to receive attention because its important role in initiating snow

100 photochemistry (McNeill et al., 2012). Anastasio and Robles (2007) first quantified the

101 light absorption of water-soluble chromophores in Arctic and Antarctic snow samples.

102 They found that ~50% of absorption for wavelength greater than 280 nm was attributed

103 to organic chromophores. Subsequently, Beine et al. (2011) determined the light

104 absorption of humic-like substances (HULIS) in snow at Barrow, Alaska. They found

105 that HULIS account for nearly half of the total absorption by dissolved chromophores

106 within the photochemically active wavelength region (300 to 450 nm), concluding that

HULIS is a major light absorber in Barrow snow and that the HULIS-mediated photochemistry is probably important for the regional environment. Several recent works have reported the radiative absorption of snow WSOC. Yan et al. (2016) estimated amount of the solar radiation absorbed by WSOC from snow collected in northern Tibetan Plateau (TP), which was 10% relative to that absorbed by BC, indicating a non-negligible role of WSOC in accelerating snow and ice melting. Similar results were also reported for WSOC extracted from other high-mountain areas (Niu et al., 2018;Zhang et al., 2019). However, chemical characterization and optical properties of the light-absorbing WSOC (aka BrC) in cryosphere is still an emerging topic. To date, no field study evaluated yet the composition-specific influence of WSOC on the snow albedo reduction.

The fluorescence excitation-emission matrix (EEM) analysis is a sensitive, rapid, and non-destructive optical spectroscopy method (Birdwell and Valsaraj, 2010) that has been used to investigate the bulk composition and attribute potential sources of chromophoric WSOC in aquatic ecosystems (Jaffé et al., 2014) and more recently in aerosols (Chen et al., 2016b, 2020;Fu et al., 2015;Mladenov et al., 2011;Wu et al., 2019b). Based on parallel factor (PARAFAC) analysis, contributions from main fluorescent components such as different fractions of HULIS and protein-like substances (PRLIS) can be quantitatively evaluated (Stedmon and Bro, 2008), indicating plausible sources of WSOC in aquatic (Murphy et al., 2008) and atmospheric samples. The chemical interpretations of PARAFAC-derived components are relatively well characterized for aquatic WSOC, but it may not be simply applied to WSOC in

snow because their sources and geochemical processes are highly different (Wu et al., 2021).

High resolution mass spectrometry (HRMS) interfaced with soft electrospray ionization (ESI) can help to decipher complexity of WSOC, providing explicit description of its individual molecular components (Qi et al., 2020). Thousands of individual organic species with unambiguously identified elemental composition can be detected at once by ESI-HRMS due to its high mass resolving power, mass accuracy, and dynamic range (Nizkorodov et al., 2011;Noziere et al., 2015). Combined with a high-performance liquid chromatography (HPLC) separation stage and photodiode array (PDA) detector, the integrated HPLC-PDA-HRMS platform enables separation of WSOC components into fractions with characteristic retention times, UV−vis spectra, and elemental composition. Correlative analysis of these multi-modal data sets facilitates comprehensive characterization of chromophores present in complex environmental mixtures (Laskin et al., 2015;Lin et al., 2016, 2018;Wang et al., 2020a). Presently, HRMS studies of WSOC exist in the cryosphere are still limited to the snow/ice in polar regions (Antony et al., 2014, 2017;Bhatia et al., 2010) and mountain glaciers in the Alps (Singer et al., 2012) and on the TP (Feng et al., 2016;Spencer et al., 2014;Zhou et al., 2019a) that with perennial snowpack. For the regions mentioned above, WSOC in snow/ice samples is dominated by proteins- or lipids-like compounds from autochthonous microbial activity with high bioavailability. Whereas, snow in northwestern China is seasonal, the snowpack persists for 3-6 months annually, and its composition is substantially influenced by local soil dust and deposited aerosols from

both natural and anthropogenic sources (Pu et al., 2017). Therefore, the chemical compositions and optical properties of WSOC from this area snowpack is likely different from those reported for the remote regions with more persistent snow coverage.

In this study, seasonal snow samples were collected across the northern Xinjiang region of China, in January 2018. We investigate the optical and molecular characteristics of WSOC using a range of analytical techniques, including UV-Vis absorption spectrophotometry, EEM, and HPLC-ESI-HRMS. Furthermore, based on the measured optical properties and concentrations of snow impurities, as well as the physical properties of snow at each site, we calculate for the first time extent of RF attributed to WSOC in snow.

2   Methods

2.1 Sample collection

28 surface and 8 subsurface sSnow samples were collected from 28 sites in Xinjiang, northwestern China during a road trip in January 2018. The area map and sampling locations are shown in Fig. 1a. The sampling sites were numbered in chronological order and with numbering scheme adopted from our previous campaigns (Pu et al., 2017;Wang et al., 2013, 2017b;Ye et al., 2012). The sampling sites were classified into four groups based on their geographical location and proximity to urban areas (Table S1): urban/industrial (U) sites (no. 106-118, and 131), rural/remote (R) sites (no. 119, 121-125, and 127-130), soil-influenced (S) sites (no.104, 105, and 126), and site 120. The U sites were located north of Tianshan Mountains, near major cities

in Xinjiang area. These sites were more likely influenced by local anthropogenic emissions (Pu et al., 2017). The rest of the sites were assigned to R group, most of them were from desert area or barren grasslands located at least ~50-100 km from major cities; hence, they were mostly influenced by natural sources. The S sites are a subgroup of the R group, they correspond to specific locations where the snowpack was visibly patchy and shallow, so local soil could be blown into snow by strong winds. For the S samples, the coarse mineral particles of yellow/brown color were clearly seen on the filters following snow water filtration (Fig. S1), consistent with the expected high loadings of soils at these sites. Out of R group, a sample from site 120 was considered separately because it showed composition and optical characteristics inconsistent with all other samples. For instance, it had very low BC concentration but highest WSOC concentration among all the samples; hence, it is discussed separately.
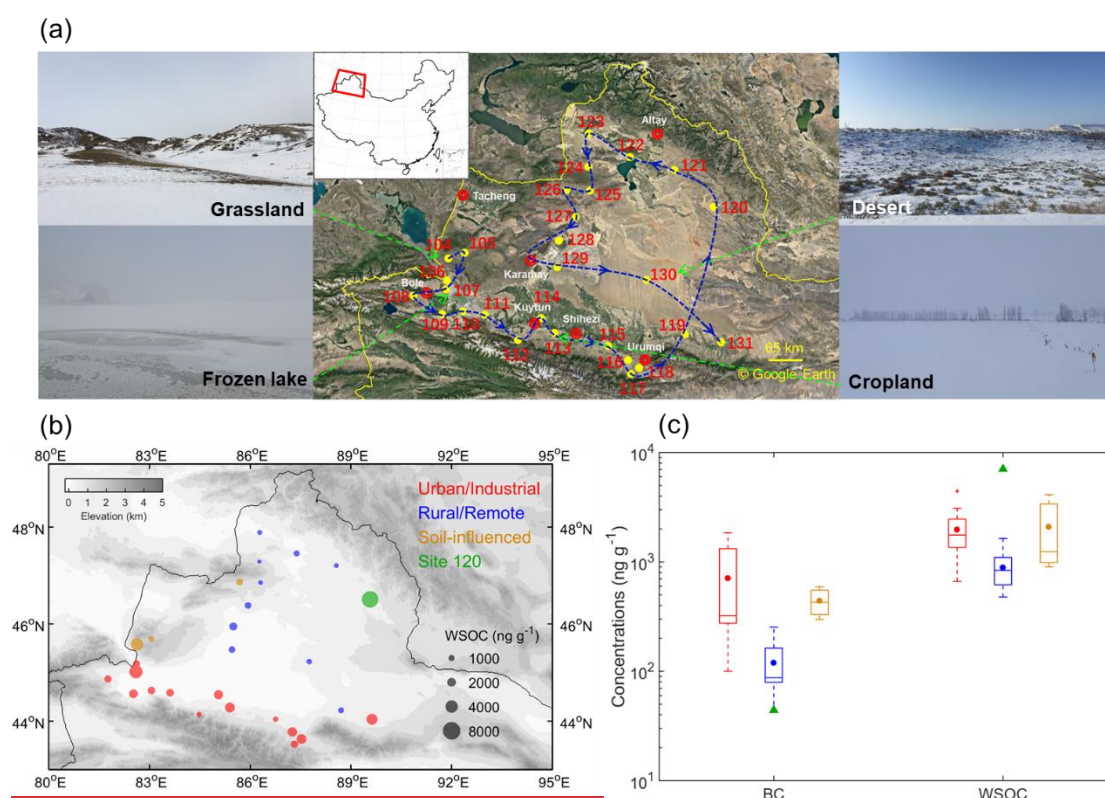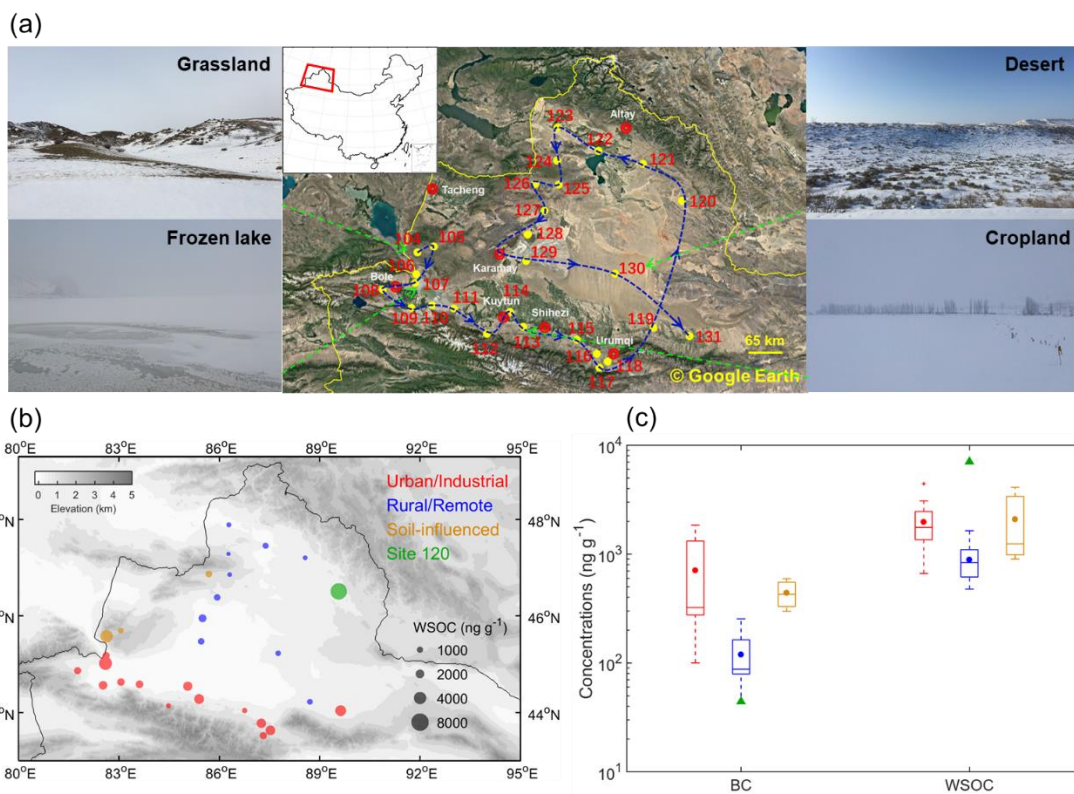
Figure 1. (a) Sampling locations and site numbers with photographs for typical land use types of sampling sites. (b) Spatial distribution of WSOC concentrations in snow. Sampling sites are divided into four groups indicated by different colors. The bubble sizes are proportional to the WSOC concentrations. (d) Variations of BC and WSOC concentrations among four groups of sites. The boxes denote the 25th and 75th quantiles, and the horizontal lines represent the medians, the averages are shown as dots; the whiskers denote the maximum and minimum data within 1.5 times the interquartile range, and the data points out of this range are marked with crosses (+).

Details of the sampling procedures can be found elsewhere (Wang et al., 2013) and they are briefly described here. The snow sampling sites were selected at least 20 km from cities and villages and at least 1 km upwind of the approach road or railway, such that the influence from single-point very local sources were minimized and the samples

199 would rather reflect conditions of large regional areas. The snow samples were

200 collected in sterile plastic bags (Whirl-Pak, Nasco, WI, USA) using clean, stainless

201 steel utensils and by scooping ~ 3 L of snow ~~every~~ on top 5 cm ~~from top to bottom~~ at

202 each site, resulting in ~600 mL volume of melted snow water. For several sites with

203 snowpack deeper than 10 cm, subsurface snow (~5-10 cm) was also collected. Snow

204 depths, snow density, and snow temperature were also measured for each sampled snow

205 layer~~snow pit~~ (Shi et al., 2020). All collected samples were then stored in a freezer (< -

206 20 °C) until further processing. 28 surface samples were analyzed by the following

207 analytical techniques.

208

209 **2.2 Chemical species analysis**

210 The snow samples were melted under room temperature and immediately filtered

211 by Polytetrafluoroethylene (PTFE) syringe filters with pore size of 0.22 μm (Thermo

212 Fisher, Inc.) to remove insoluble solids. Obtained filtrates were then used for the

213 measurements of concentrations of soluble inorganic ions, mass loadings of WSOC,

214 acquisition of bulk UV-Vis absorption and EEM spectra, and molecular characterization

215 using HPLC-ESI-HRMS platform.

216 The major inorganic ions (Na^+, NH_4^+, K^+, Mg^{2+}, Ca^{2+}, Cl^-, SO_4^{2-}, and NO_3^-)

217 were measured by an ion chromatography system (Dionex 600, Thermo Scientific, MA,

218 USA) using an IonPac AS22 column for anions and an IonPac CS12A column for

219 cations. The detection limits for all inorganic ions are greater than 0.05 mg L^{-1}. The

220 concentrations of WSOC were analyzed by a total organic carbon analyzer (Aurora

1030W, OI Analytical, TX, USA). Each measurement was done in triplicate, the average ~~values~~ concentrations of ~~each~~ four groups of samples and the values for each sample after blank subtraction are presented in Tables S2 and S3~~1, respectively~~. The detection limit and relative standard deviation of measurements were 2 ppb and 1%, respectively.

The BC concentrations in snow were measured by a custom-developed two-sphere integration (TSI) spectrophotometer (Wang et al., 2020b), and have been reported by Shi et al. (2020). The distribution of BC concentrations in snow samples is also shown in Fig. S2.

2.3 UV-Vis absorption and fluorescence EEM spectroscopic measurements

The UV-Vis absorption and fluorescence EEM spectra were recorded simultaneously by an Aqualog spectrofluorometer (Horiba Scientific, NJ, USA) in a 1 cm quartz cuvette. The excitation wavelengths for EEM were 240 to 600 nm in intervals of 5 nm and were the same for UV-Vis spectrum acquisition. The fluorescence emission range was 250 to 825 nm in 5 nm intervals with an integration time of 0.5 s. An ultrapure water (18.2 MΩ cm, Milli-Q purification system, Millipore, Bedford, MA, USA) was used for blank measurement, subtracted from all sample spectra.

The absorbance at 600 nm was subtracted from the whole spectrum to correct the scattering effects and baseline shifts of the instrument (Chen et al., 2019). The BrC mass absorption coefficients (MAC; m^2 g^{-1}) related to WSOC contributions were calculated by:

$$MAC_{BrC}(\lambda) = \frac{\ln(10) \cdot A(\lambda)}{c_{\text{WSOC}} \cdot L} \tag{1}$$

243   Where λ is the wavelength, A is the base-10 absorbance measured by the

244   spectrophotometer, C_{WSOC} (mg L^{-1}) is the concentration of WSOC, L is the cuvette path

245   length (0.01 m). To characterize the wavelength dependence of MAC_{BrC}, absorption

246   Ångström exponents (AAE) were determined by a power-law regression (Kirchstetter

247   et al., 2004):

248    $MAC(\lambda)= k \cdot \lambda^{-AAE},$ (2)

249   where k is a constant related to WSOC concentrations. To exclude absorption due to

250   inorganic chromophores (e.g., nitrate), the AAE values were derived from the power

251   law fits limited to the range of 330- 400 nm ($AAE_{330-400}$) (Yan et al., 2016).

252   Processing of the EEM data followed the protocols described elsewhere (Zhou et

253   al., 2019b). Briefly, the raw EEM data sets were first background subtracted to remove

254   the water Raman scatter peaks, then the inner filter effect was corrected (Kothawala et

255   al., 2013). The fluorescence intensities were normalized to water Raman unit (RU)

256   (Lawaetz and Stedmon, 2009). The processed EEM data was analyzed by the

257   PARAFAC model in the manner similar to our previous report (Zhou et al., 2019b). In

258   this study, the PARAFAC modeling was conducted using drEEM toolbox (version 0.2.0,

259   http://models.life.ku.dk/drEEM) (Murphy et al., 2013). According to the analysis of

260   residual errors of 2- to 7- component models and split half analysis, a 3-component

261   model was selected. Only 2- and 3-component models have passed the split-half

262   analysis with the "S4C6T3" split scheme (Fig. S3) (Murphy et al., 2013). Moreover,

263   the sum of residual error decreased significantly when the number of components

264   increased from 2 to 3 (Fig. S4). The spectra of derived fluorescent components appeared

265 consistent with those commonly found in other studies (Table S~~4~~2).

2.4 HPLC-ESI-HRMS Molecular Analysis and data processing

The WSOC extracts were desalted and concentrated through solid phase extraction (SPE) method using DSC18 cartridges (Supelco, Millipore Sigma, PA, USA). The cartridges were conditioned and equilibrated by one-column volume (~3 mL) of acetonitrile (ACN, Optima, LC-MS grade, Fisher Scientific Inc.) and one-column volume of water (Optima, LC-MS grade, Fisher Scientific Inc.), respectively. To increase the efficiency of SPE, the sample was acidified to pH ≈ 2 using HCl (Lin et al., 2010), and 3 mL of acidified sample flowed through the cartridge at a low flow rate of 1-2 drops per second. Salts and other unretained compounds (e.g., small molecular acids and carbohydrates) were first washed out by one-column volume of water, and the analyte retained on the cartridge was then eluted by two-column volumes of ACN. The efficiency of SPE was evaluated by measuring the UV-Vis absorption before and after elution and ensured the good recovery of analytes (Text S1). The ACN eluents were concentrated to 150 μL under a gentle stream of pure N_2, and then diluted by adding 150 μL of ultrapure water. Finally, the reconstituted extracts were ~~blown down~~further concentrated to 200 μL prior to HPLC analysis.

The obtained extracts were analyzed using a Vanquish HPLC system coupled to a Q Exactive HF-X Orbitrap HRMS with an IonMAX ESI source (all from Thermo Scientific Inc.). The HPLC separation was performed on a Phenomenex Luna C18 revised-phase column (2 mm × 150 mm, 5 μm particles, 100 Å pores). A gradient elution was performed at a flow rate of 200 μL/min by an A + B binary mobile phase

system: (A) water with 0.05% v/v formic acid and (B) acetonitrile with 0.05% v/v

formic acid (Optima, LC-MS grade, Fisher Scientific Inc.). The elution protocol was

0−3 min hold at 90% A, 3−90 min linear gradient to 0% A, 90-100 min hold at 0% A,

and then 100−130 min hold at 90% A to recondition the column for the next sample.

The column temperature was maintained at 25 °C and the sample injection volume was

25 μL. The UV-vis absorption of eluted chromophores was recorded by a PDA detector

over the wavelength range of 200 to 700 nm. Correlation analysis between PDA and

MS peaks and relative absorption of different chromophore fractions will be discussed

in an upcoming paper. For ESI-HRMS analysis, the following settings were used: 45

units of sheath gas, 10 units of auxiliary gas, 2 units of sweep gas, a spray voltage of

3.5 kV, a capillary temperature of 250 °C, and a sweep cone was used. The mass spectra

were acquired at a mass range of 80–1,200 Da at mass resolving power of $\Delta m/m =$

240,000 at m/z 200. Mass calibration was performed using commercial calibration

solutions (PI-88323 and PI-88324, Thermo Scientific) for ESI(+/-) modes.

The raw experimental data files were acquired by Xcalibur software (Thermo

Scientific Inc.). The HPLC-ESI-HRMS data sets were preliminary processed using an

open source software toolbox, MZmine 2 (http://mzmine.github.io/), to perform peak

deconvolution and chromatogram construction (Myers et al., 2017;Pluskal et al., 2010).

The background subtraction and formula assignment were performed using customized

Microsoft Excel macros (Roach et al., 2011). The formulas were assigned based on

first- and second-order Kendrick mass defects and a MIDAS formula calculator

(http://magnet.fsu.edu/~midas/). $[M + H]^+$, $[M + Na]^+$, and $[M − H]^−$ ions were assumed

309   to identify products detected in ESI+ and ESI- modes, respectively. Besides, adduct

310   ions were also identified and removed using a homemade MATLAB script (Text S2).

311   The molecular formulas were assigned using the following constraints: $1 \leq C \leq 50$, $1 \leq$

312    $H \leq 100$, $N \leq 5$, $O \leq 50$, $S \leq 1$, and $Na \leq 1$ (ESI+ only) and mass tolerance of <3.0 ppm.

313   Furthermore, to eliminate the formulas not likely to be observed in nature, the elemental

314   ratio limits of $0.3 \leq H/C \leq 3.0$, $0.0 \leq O/C \leq 3.0$, $0.0 \leq N/C \leq 1.3$, $0.0 \leq S/C \leq 0.8$ (Lin

315   et al., 2012;Wang et al., 2018) were applied. The double-bond equivalent (DBE) values

316   of the neutral assigned species $C_cH_hO_oN_nS_s$ were calculated using the equation:

317    $DBE = c - \frac{h}{2} + \frac{n}{2} + 1$ (3)

318   The aromaticity index (AI) is a conservative criterion for the unequivocal identification

319   of aromatic and condensed aromatic structures in natural organic matter calculated as

320   (Koch and Dittmar, 2006, 2016):

321    $AI = \frac{1 + c - o - s - 0.5(h+n)}{c - o - n - s}$,   (4)

322    $AI > 0.5$ and $AI \geq 0.67$ are unambiguous minimum thresholds for the presence of

323   aromatic and condensed aromatic structures in a molecule, respectively. If either the

324   numerator or denominator in Eq. (4) equals to 0, then AI is assigned with 0 value.

325   The intensity (I^*) weighted molecular weight (MW_w) and other characteristic

326   molecular parameters of H/C (H/C_w), O/C (O/C_w), DBE (DBE_w), DBE/C (DBE/C_w), and

327   AI (AI_w) were calculated using Eq. (5):

328    $X_w = \frac{\sum(I_i^* \cdot X_i)}{\sum I_i^*}$,   (5)

329   where X_w represents any of the weighted parameters introduced above; I_i^*, and X_i are

330   the corresponding intensity and the molecular parameter values calculated for each

331 assigned species i, respectively.

2.5 Snow Albedo Modeling and Radiative Forcing Calculations

333 The spectral snow albedo was calculated by the Snow, Ice, and Aerosol Radiative

334 (SNICAR) model (Flanner et al., 2007), which accounts for the radiative transfer in the

335 snowpack based on the theory from Wiscombe and Warren (1980) and the two-stream,

336 multilayer radiative approximation (Toon et al., 1989). The input parameters required

337 for the SNICAR model are snow depth, snow density, effective snow grain size, solar

338 zenith angle, and impurity concentrations. Snow depth and density were measured in

339 the field. The effective snow grain size was retrieved from the ~~filed measured~~ spectral

340 albedo measured in the field, and detailed information can be found in our previous

341 study (Shi et al., 2020). The solar zenith angle was calculated using the site location

342 and sampling date for each site. The input values of parameters for the SNICAR model,

343 which are those for surface snow, are summarized in Table S5~~3~~. For simplicity, a

344 homogenous snowpack assumption was applied for both snow physical properties and

345 pollutants concentrations.

346 To evaluate influence of BrC attributed to WSOC on the snow albedo, optical

347 properties of BrC material such as single scattering albedo (SSA), asymmetry factor (g),

348 and mass extinction coefficient (MEC) are needed as inputs for simulation. These

349 parameters were calculated by Mie theory, approximating WSOC as an ensemble of

350 small BrC particles distributed evenly in the snowpack. The input variables required

351 for Mie calculation are complex refractive index ($RI = n - ik$) and particle size parameter

352 ($x = \pi d/\lambda$). The diameter of individual particles (d), density (ρ), and the real part (n) of

353 *RI* of WSOC were assumed to be 150 nm, 1.2 g cm^{-3}, and 1.55 (constant in the UV-Vis

354 range), respectively (Chen and Bond, 2010;Lu et al., 2015b). The imaginary part (*k*) of

355 *RI* was calculated as (Sun et al., 2007):

356 $k(\lambda) = \frac{MAC \cdot \rho \cdot \lambda}{4\pi}.$ (6)

357 Then, *SSA*, *g*, and extinction cross-section (*Q$_{ext}$*) were derived from Mie code

358 (https://omlc.org/software/mie/), and the obtained values were then used to calculate

359 *MEC* as (Seinfeld and Pandis, 2016):

360 $MEC = \frac{\pi d^2/4 \cdot Q_{ext}}{\pi d^3/6 \cdot \rho}.$ (7)

361   The spectral albedo (*α$_\lambda$*) was calculated for the scenarios of pure snow and BC/BrC-

362 contaminated snow. After that, the broadband albedo (*α*) of each scenario needs to be

363 determined to calculate the broadband albedo reduction (Δ*α*) and *RF* due to different

364 types of impurities. *α* was derived by integration of *α$_\lambda$* over the wavelength range of 300

365 to 1500 nm weighted by the incoming solar irradiance *S*(*λ*).

366 $\alpha = \frac{\int_{300}^{1500} \alpha_\lambda S(\lambda) d\lambda}{\int_{300}^{1500} S(\lambda) d\lambda}.$ (8).

367 The incoming solar irradiance were simulated by Coupled Ocean-Atmosphere

368 Radiative Transfer (COART) model (https://cloudsgate2.larc.nasa.gov/jin/coart.html)

369 (Jin et al., 2006) for each site under clear sky assumption, therefore the calculated *RF*

370 can be considered as upper limits.

371 The *RF* resulted from either BC or BrC in snow (*RF$_{BC,BrC}$*) were calculated by

372 multiplying the downward shortwave solar radiation flux at surface by Δ*α$_{BC,BrC}$* (Painter

373 et al., 2013):

374 $RF_{BC,BrC} = E \cdot \Delta\alpha_{BC,BrC},$ (9)

375 $\Delta\alpha_{BC,BrC} = (\alpha_{pure\ snow} - \alpha_{BC,BrC})$, (10)

376 where E is the average-daily downward shortwave solar radiation flux acquired from

377 NASA's Clouds and the Earth's Radiant Energy System (CERES) product "CERES

378 SYN1deg" (https://ceres.larc.nasa.gov/products.php?product=SYN1deg). $\alpha_{pure\ snow}$ and

379 $\alpha_{BC,BrC}$ are the broadband albedo of pure snow and BC or BrC contaminated snow,

380 respectively.

381

382 **3 Results and Discussions**

383 **3.1 Characteristics of chemical species**

384 Figure 1b shows mass concentrations of WSOC measured in the snow samples,

385 illustrating their broad range from 478 to 7069 ng g^{-1} with an average of 1775±1424 ng

386 g^{-1} (arithmetic mean ± 1 standard deviation, and same below). The U and the S sites

387 showed higher concentrations with averages of 1968±953 ng g^{-1} and 2082±1438 ng g^{-}

388 ^{1}, respectively, while the value of R sites (885±328 ng g^{-1}) was approximately a factor

389 of two lower (Table S2̶1̶). Of note, the WSOC concentrations in U and S samples

390 reported here are significantly higher than those found in the snow and ice from polar

391 regions (~40 – 500 ng g^{-1}) (Fellman et al., 2015;Hagler et al., 2007a, b;Hood et al.,

392 2015), glaciers on the European Alps (~100 – 300 ng g^{-1}) (Legrand et al., 2013;Singer

393 et al., 2012), and the remote TP region (~150 – 700 ng g^{-1}) (Yan et al., 2016). However,

394 our reported WSOC mass concentrations are in the same range as those in the fresh

395 snow samples collected from Laohugou (LHG) glacier, northern TP (2000 – 2610 ng g^{-}

396 ^{1}) (Feng et al., 2018). It has been reported that glaciers and ice sheets from polar or

alpine regions store a large amount of WSOC and discharge it to their downstream terrestrial ecosystems (Hood et al., 2009, 2015;Singer et al., 2012). Comparable or even higher concentrations of WSOC in our samples indicate that ~~It follows that in addition to the snow and glaciers from polar or alpine regions,~~ the seasonal snow in Northern Xinjiang is also an important organic carbon source for the terrestrial~~covered~~ ecosystems during spring meltdown.

As shown in Fig. 1c, the U sites were also associated with the highest BC concentrations among all four groups (mean: 707 ± 651 ng g^{-1}). Furthermore, the mass contributions of sulfate ions at U sites (Table S2$\cancel{1}$, mean: $33\%\pm7\%$), which is a commonly-used marker for fossil fuel burning (Pu et al., 2017), were approximately twice as high as those from the other sites. All these results indicate strong influence from anthropogenic pollution sources, explaining high WSOC loadings at U sites. For the S sites, HULIS from local soil may dominate the WSOC composition. For example, snow at site 104 was patchy and thin (Fig. 1a, grassland), the local black soil can be lifted by winds and then redeposited and mixed with snow. The assumption of soil contributions agrees with observed high mass contribution of calcium ions in S samples (mean: $50\%\pm4\%$, see Table S2$\cancel{1}$). Although WSOC concentrations in R samples were relatively low $(885\pm328$ ng g$^{-1})$, they were still higher than most of the values from high-altitude or high-latitude regions of previous studies $(\sim40 - 700$ ng g^{-1} as mentioned in the last paragraph). It might be explained by two reasons: (1) more intensive anthropogenic emissions in the northern Xinjiang region; (2) there was little snowfall during 2018 campaign; therefore, ~~pollutants~~ WSOC had been potentially accumulated

419 on the snow surface by sublimation and dry deposition (Doherty et al., 2010). The

420 sample from site 120 is discussed separately as it exhibited the highest WSOC

421 concentration (7069 ng g^{-1}) and almost the lowest BC concentration (44 ng g^{-1}) out of

422 all samples analyzed in this work. The potential sources of WSOC from site 120 sample

423 will be discussed in section 3.3.

424

3.2 Bulk light-absorbing and fluorescence properties

426 The average MAC_{BrC} spectra of WSOC from different groups of samples are shown

427 in Fig. 2a. The average MAC_{BrC} at 365 nm (MAC_{365}) of S samples (0.94±0.31 m^2 g^{-1})

428 was significantly higher than those of U (0.39±0.11 m^2 g^{-1}) and R (0.38±0.12 m^2 g^{-1})

429 samples, respectively (Table S2~~1~~). The information on MAC_{BrC} related to WSOC in

430 snow and ice is yet very scarce in literature. The MAC_{365} values of U and R samples are

431 comparable with the results reported for continental snow collected ~~from~~across ~~Barrow,~~

432 Alaska (0.37~~2~~±0.32~~24~~ m^2 g^{-1}) (Zhang et al., 2020), but slightly lower than those of snow

433 WSOC from Chinese Altai Mountains, which shows a wide range from ~0.3 m^2 g^{-1} for

434 accumulation season to ~1.0 m^2 g^{-1} for ablation season with an average of (~~0.45±0.35~~

435 ~~m^2 g^{-1}~~) (Zhang et al., 2019), and HULIS extracted from Arctic snow (~0.5 m^2 g^{-1})

436 (Voisin et al., 2012). The snow/ice samples from LHG glacier on the TP (Yan et al.,

437 2016) presented a higher average MAC_{365} (1.3 – 1.4 m^2 g^{-1}) than the S samples; they

438 also indicated large contribution of dust-derived organics. The relative lower values of

439 MAC_{365} measured for U samples might be explained by photobleaching of WSOC

440 during aging on the snow surface (Yan et al., 2016;Zhang et al., 2019). Due to the

441 stronger wavelength dependence of WSOC from U samples ($AAE_{330-400}$: 6.0±0.8 vs.

442 5.4±0.7 for U and R sites, respectively), their *MAC* values at shorter wavelength of 300

443 nm were higher compared to those of R samples. For example, the averages of MAC_{300}

444 were 1.32±0.24 m^2 g^{-1} and 1.02±0.21 m^2 g^{-1} for U and R samples, respectively (Table

445 S2~~1~~). The $AAE_{330-400}$ of our samples were in the range of 4.3 to 12.3 (mean: 6.0±1.5),

446 and S sites had a higher average of 6.4±0.3 than those corresponding to U and R samples.

447 The highest $AAE_{330-400}$ = 12. 3 was found for WSOC from site 120 sample, and its UV-

448 Vis spectrum also exhibited an unusual spectral shape with a well-defined spectral

449 feature observed between 300 and 350 nm. Similar feature was reported in: (1)

450 cryoconite samples collected from TP glaciers (Feng et al., 2016), which may be

451 attributed to mycosporine-like amino acids (MAAs) produced by microorganisms (e.g.

452 fungi, bacteria, and algae) (Elliott et al., 2015;Shick and Dunlap, 2002); (2) Plant-

453 derived (e.g., corn, hairy vetch, or alfalfa) water extractable organic matter containing

454 phenolic carboxylic compounds (He et al., 2009).

455
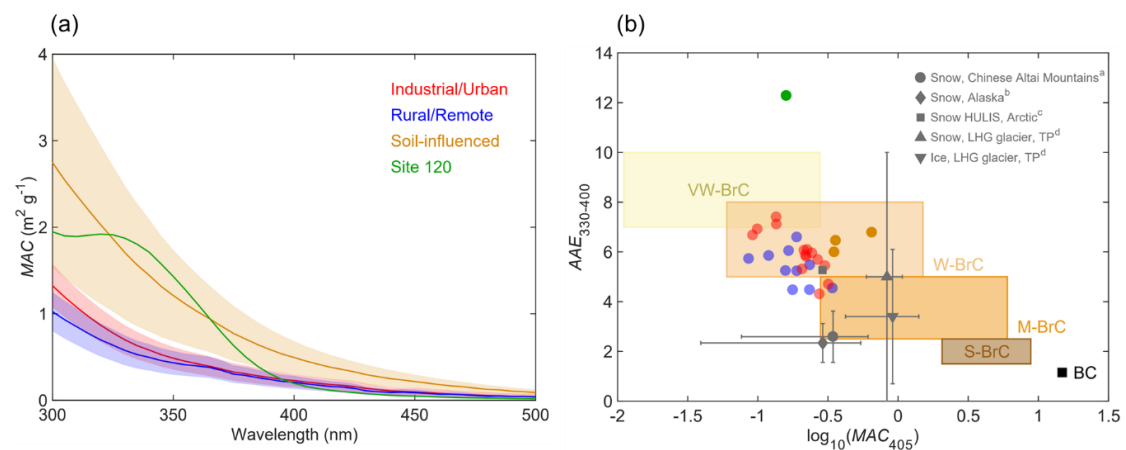
456 **Figure 2.** (a) The average *MAC* spectrum of BrC attributed to WSOC in each group (solid lines,

457 denoted by different colors), the shaded areas represent one-time standard deviations. (b) Plot of the

458 optical-based BrC classification scheme (Saleh, 2020) in the $\log_{10}(MAC_{405}) - AAE_{330-400}$ space. The

shaded areas represent very weakly absorbing BrC (VW-BrC), weakly absorbing BrC (W-BrC),

moderately absorbing BrC (M-BrC), and strongly absorbing BrC (S-BrC). BC is also shown for

reference (Bond and Bergstrom, 2006). Grey marks indicate the data from literatures for snow/ice

samples from Chinese Altai Mountains ([a] Zhang et al., 2019), Alaska ([b] Zhang et al., 2020), Arctic

([c] Voisin et al., 2012, AAE is calculated for 300-400 nm), LHG glacier on the TP ([d] Yan et al., 2016).

Error bars denote the standard deviations of AAE or MAC values.

Figure 2b shows MAC and $AAE_{330\text{-}400}$ values measured for BrC attributed to WSOC

from our samples in the context of an optical-based classification of BrC presented

recently by Saleh (2020). The optical properties characterizing the BrC classes are

expected to be associated with their corresponding physicochemical properties (i.e.

molecular sizes, volatility, and solubility). Most of our samples and HULIS in Arctic

snow (Voisin et al., 2012) fall into the region of weakly absorbing BrC (W-BrC). The

WSOC in snow/ice from Alaska, Chinese Altai Mountains, and LHG glaciers were

assigned to moderately absorbing BrC (M-BrC) but with broader ranges, likely

indicating higher molecular variability. These results provide a useful ~~framework~~

dataset ~~for~~ of ~~representing~~ snow BrC ~~optical~~ light-absorbing properties which ~~in~~ may

inform climate models.

Three fluorescent components (i.e., C1, C2, and C3) were identified by PARAFAC

analysis (Fig. 3a). The peak positions of each component are summarized in Table S4~~2~~.

C1 (HULIS-1) is a type of terrestrial-derived humic fluorophore with long emission

wavelengths, commonly reported for samples of terrestrial aquatic systems and highly-

481 oxygenated organic aerosols (Chen et al., 2016a;Stedmon et al., 2003). C2 (HULIS-2)

482 is usually recognized as HULIS from marine sources (Coble, 1996) or phytoplankton

483 degradation in fresh water (Zhang et al., 2010), and it was also detected in

484 anthropogenic wastewater (Stedmon and Markager, 2005) or industrial-sourced aerosol

485 (Chen et al., 2020). C3 is a class of PRLIS (tyrosine-like) widely found in terrestrial

486 organics (Wu et al., 2020;Zhang et al., 2010;Zhao et al., 2016) related to labile organic

487 matter produced from microbial processes (Coble et al., 1998). Of note, the

488 fluorophores detected in our samples show the similar peak positions compared to the

489 previous reports for aerosol or aquatic environments, but they do not necessarily have

490 the same sources due to large differences of the physicochemical and geochemical

491 processes (Chen et al., 2016b;Duarte et al., 2007).

492
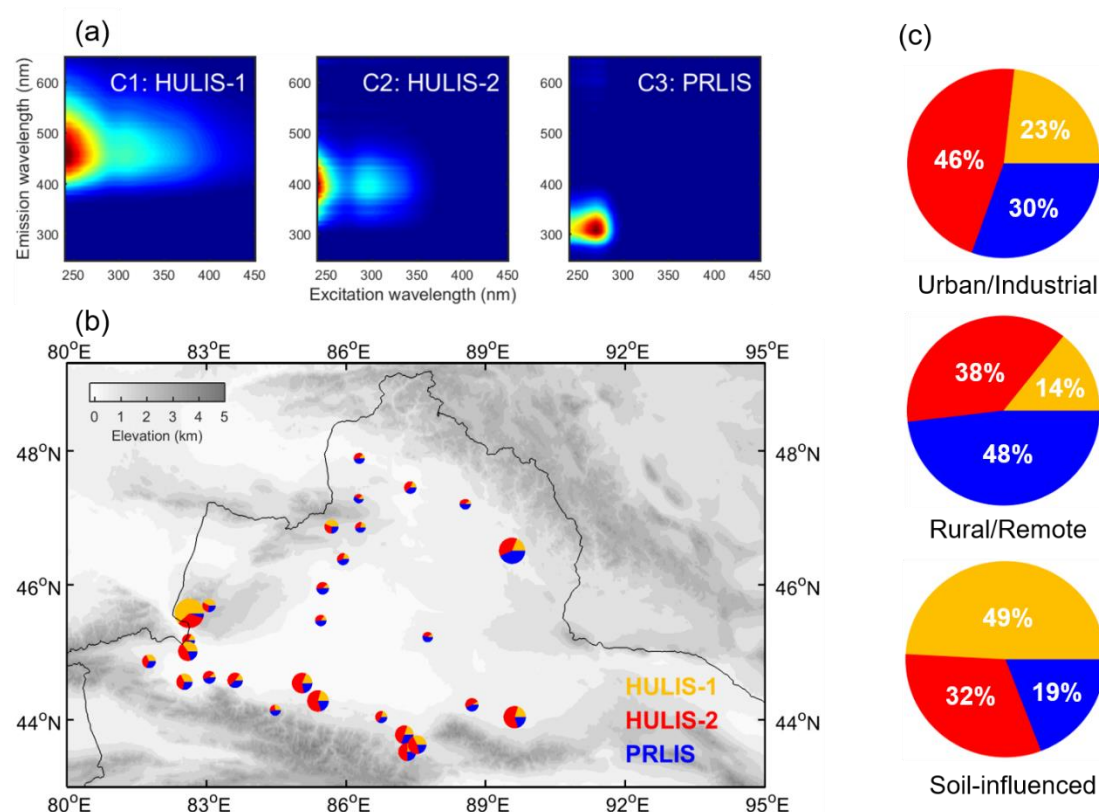
Figure 3. (a) The fingerprints of three fluorescent components identified by PARAFAC analysis. (b)

Relative contributions of three components to total fluorescence at each site. HULIS-1, HULIS-2,

and PRLIS are represented in yellow, red, and blue, respectively. The size of each pie is proportional

to the total fluorescence intensity at each site. (c) The average contributions of three components in

different groups of samples.

As shown in Figs. 3b and 3c, the relative intensities of three fluorescent

components were highly variable among different groups of samples, suggesting

systematic substantial differences in their chemical compositions. HULIS-1 dominates

in the S samples, where it accounts for ~49% of the total fluorescence (Table S2~~1~~). In

addition, the relative intensities of HULIS-1 are positively correlated with the mass

fractions of calcium ion (r=0.73, p<0.01, Table S6~~4~~). These results suggest terrestrial

origin (soil dust) of HULIS-1, which is consistent with previous studies of water

systems and aerosols (Chen et al., 2016a, 2020;Stedmon et al., 2003). A strongly

negative correlation between the contributions of HULIS-1 and nitrate mass fractions

is found as well (r=-0.68, p<0.01), reflecting the potential important role of HULIS in

snow nitrate photochemistry (Handley et al., 2007;Yang et al., 2018) ~~(Bartels-Rausch~~

~~et al., 2010;Grannas et al., 2007)~~. For instance, Yang et al. (2018) found that HONO

formation is significantly enhanced, in the presence of humic acid, from nitrate

photolysis. HULIS-2 dominates U samples with an average contribution of ~46%.

Given the significantly positive correlation between the contributions of HULIS-2 and

mass fractions of sulfate ion (r=0.51, p<0.01), the primary relevance of anthropogenic

emissions for HULIS-2 is confirmed. The R samples show significant contribution of PRLIS fluorophore (mean: 48%±6%), indicating an important role of microbial processes in the composition of WSOC in these samples. This observation is in line with previous studies showing that snow is not only an active photochemical site, but also a biogeochemical reactor in the nitrogen cycling (Amoroso et al., 2010). Amoroso et al. (2010) found that nitrate and nitrite ions in snow collected from Ny-Ålesund, Norway, were most likely from microbial oxidation of ammonium ions. Therefore, the significant correlation (r=0.78, p<0.01) between relative intensities of PRILS and nitrate mass fractions might be interpreted by: (1) low anthropogenic emissions and local soil dust import (Less contributions of sulfate and calcium ions) and (2) potential metabolic production of nitrate/nitrite in snow at R sites. Further research is needed to investigate this hypothesis in more detail. Of interest, EEM from site 120 sample cannot be modeled well by PARAFAC (Fig. S5) because of the uncommon spectroscopic feature with emission and excitation wavelengths of 315 nm and 452 nm, respectively. This feature is possibly attributed to: (1) NADH (Nicotinamide adenine dinucleotide) - like compounds, which is an indicator for the metabolism of organisms (Pöhlker et al., 2012) or (2) plant-derived water extractable organic matter (Hunt and Ohno, 2007), e.g., corn. This result suggests strong influence from either microbial activity or plant-sourced organics in snow at site 120, which is also consistent with the UV-Vis spectrum shape.

3.3 Molecular-level insights into composition of WSOC from snow samples

3.3.1 General HRMS characteristics

Numbers of assigned species ranged from 561 to 1487 and from 339 to 1568 for ESI+ and ESI- modes, respectively, suggesting high variations of molecular components of WSOC in the snow samples from northern Xinjiang. The assigned peaks accounted for majority (49% - 68%) of all detected MS peaks. Due to the different ionization mechanisms between positive and negative ESI (Lin et al., 2012), only small amounts of compounds were detected in both modes, accounting for approximately 15% of total assignments at each representative site (Fig. S6). The assigned formulas were classified into eight categories, i.e., CHO, CHON, CHOS, CHONS, CH, CHS, CHN, CHS. CHONS referred to formulas containing carbon, hydrogen, oxygen, nitrogen and sulfur elements, and other categories were defined analogously. The U samples had the highest number of assigned compounds among four groups of sites in both ESI+ and ESI- with averages of 1113±203 and 871±287, respectively (Tables 1 and 2), whereas the number of assigned species from S samples were lowest (mean: 727±146 and 438±84 for ESI+ and ESI- modes, respectively), reflecting high molecular complexity of U samples. The numbers of assigned formulas in this study are comparable with the assignments reported for urban aerosol samples (~800-1800) (Lin et al., 2012;Wang et al., 2017a) and WSOC of LHG glacier from the TP region (~700-1900) (Feng et al., 2016, 2018), but they are lower than those of WSOC from Antarctica (~1400-2600) and Greenland ice sheets (~1200-4400) (Antony et al., 2014;Bhatia et al., 2010).

558 **Table 1.** Averages (Arithmetic Mean ± Standard Deviation) of molecular characteristics in major formula categories detected in ESI+ mode for each group of sites.

559 Numbers and percentages of formulas, intensity weighted MW_w, H/C_w, O/C_w, DBE_w, DBE/C_w, AI_w are given.

		All+	CH+	CHO+	CHON+	CHOS+	CHONS+	CHS+
	Number of formulas	1113±203	48±6	460±68	249±61	121±33	135±45	43±15
	Percent of formulas (%)		4.4±10.5	42.9±5.4	22.1±1.4	110.8±21.8	121.9±2.3	43.8±1.2
U	Molecular weight (Da)	231±9	146±5	207±21	211±15	329±18	294±18	257±13
Urban/Industrial	H/C_w	1.51±0.05	1.31±0.04	1.72±0.10	1.73±0.14	1.12±0.09	1.70±0.08	1.11±0.02
(n = 14)	O/C_w	0.19±0.04	0	0.28±0.05	0.23±0.02	0.07±0.02	0.29±0.04	0
	DBE_w	5.08±0.60	4.6±0.47	3.03±0.66	3.68±0.68	10.13±0.70	4.10±0.44	8.67±0.63
	DBE/C_w	0.34±0.03	0.44±0.02	0.24±0.04	0.34±0.07	0.49±0.05	0.35±0.04	0.51±0.01
	AI_w	0.25±0.04	0.44±0.02	0.13±0.03	0.17±0.09	0.42±0.07	0.15±0.04	0.48±0.01
	Number of formulas	942±166	45±11	533±81	245±51	25±15	53±13	7±3
	Percent of formulas (%)		54.7±10.8	576.8±21.9	265.9±1.52	2.63±1.52	5.66±1.1	0.7±0.2
R	Molecular weight (Da)	229±10	134±11	239±12	214±17	351±21	260±20	237±30
Remote/Rural	H/C_w	1.69±0.04	1.26±0.08	1.75±0.04	1.69±0.10	1.51±0.04	1.74±0.08	1.17±0.12
(n = 10)	O/C_w	0.34±0.01	0	0.39±0.01	0.27±0.02	0.10±0.05	0.26±0.02	0
	DBE_w	3.16±0.21	4.53±0.31	2.80±0.16	4.11±0.48	6.25±0.51	3.92±0.62	7.49±1.64
	DBE/C_w	0.26±0.02	0.47±0.04	0.22±0.02	0.35±0.05	0.30±0.02	0.39±0.03	0.49±0.06
	AI_w	0.12±0.03	0.47±0.04	0.07±0.03	0.18±0.06	0.19±0.03	0.15±0.04	0.45±0.07
	Number of formulas	727±146	27±11	407±106	186±39	34±21	33±4	7±6
	Percent of formulas (%)		3.74±0.91	55.56±4.0	25.66±0.3	5.0±3.0	4.85±1.21	1.0±0.91
S	Molecular weight (Da)	218±15	138±3	215±30	188±14	330±11	290±20	220±32
Soil-influenced	H/C_w	1.73±0.05	1.33±0.02	1.84±0.08	1.75±0.06	1.35±0.17	1.73±0.06	0.92±0.13
(n = 3)	O/C_w	0.33±0.04	0	0.40±0.01	0.23±0.01	0.07±0.01	0.29±0.05	0
	DBE_w	3.11±0.45	4.29±0.13	2.21±0.53	3.31±0.06	7.60±1.56	4.23±0.18	8.63±0.34
	DBE/C_w	0.25±0.03	0.44±0.01	0.18±0.03	0.32±0.03	0.38±0.09	0.36±0.02	0.61±0.07
	AI_w	0.14±0.05	0.44±0.01	0.07±0.02	0.15±0.03	0.29±0.09	0.13±0.03	0.58±0.07
Site **120**	Number of formulas	987	51	578	238	10	65	4

	(n = 1)						
Percent of formulas (%)		5.2	59.6	24.1	1.0	76.6	0.4
Molecular weight (Da)	234	145	245	212	338	246	250
H/C_w	1.69	1.29	1.72	1.80	1.54	1.95	1.14
O/C_w	0.32	0	0.37	0.26	0.06	0.29	0
DBE_w	3.36	4.67	3.14	3.54	5.87	2.99	8.05
DBE/C_w	0.26	0.45	0.23	0.30	0.28	0.32	0.50
AI_w	0.11	0.45	0.07	0.12	0.20	0.07	0.46

560
561 **Table 2.** Averages (Arithmetic Mean ± Standard Deviation) of molecular characteristics in major formula categories detected in ESI- mode for each group of sites.

562 Numbers and percentages of formulas, intensity weighted MW_w, H/C_w, O/C_w, DBE_w, DBE/C_w, AI_w are given.

		All-	CHO-	CHON-	CHOS-	CHONS-
U Urban/Industrial (n = 14)	Number of formulas	871±287	404±112	194±79	156±48	82±49
	Percent of formulas (%)		47.2±3.64	21.92±2.2	18.2±21.9	98.7±3.2
	Molecular weight (Da)	223±17	229±19	183±18	238±17	252±24
	H/C_w	1.48±0.09	1.57±0.06	1.00±0.14	1.68±0.08	1.55±0.15
	O/C_w	0.35±0.04	0.30±0.05	0.45±0.04	0.56±0.05	0.60±0.06
	DBE_w	4.14±0.26	3.87±0.31	5.59±0.51	3.13±0.42	4.55±0.55
	DBE/C_w	0.38±0.06	0.30±0.04	0.72±0.08	0.29±0.04	0.46±0.08
	AI_w	0.19±0.07	0.12±0.04	0.54±0.09	0.05±0.02	0.14±0.06
R Rural/Remote (n = 10)	Number of formulas	537±92	266±35	107±21	100±29	34±16
	Percent of formulas (%)		50.0±4.0	20.9±21.9	18.3±2.3	6.0±2.2
	Molecular weight (Da)	215±21	216±28	180±12	241±22	241±27
	H/C_w	1.44±0.07	1.54±0.10	1.03±0.16	1.76±0.10	1.52±0.13
	O/C_w	0.39±0.06	0.37±0.07	0.42±0.04	0.58±0.08	0.65±0.07
	DBE_w	4.09±0.31	3.70±0.65	5.43±0.69	2.68±0.86	4.30±0.79
	DBE/C_w	0.42±0.05	0.33±0.05	0.72±0.10	0.25±0.06	0.49±0.07
	AI_w	0.26±0.05	0.13±0.05	0.60±0.14	0.04±0.04	0.16±0.06
S	Number of formulas	438±84	245±53	85±18	69±9	22±6

Soil-influenced (n = 3)						
Percent of formulas (%)		565.6±2.0	19.3±10.8	16.1±2.2	5.0±10.7
Molecular weight (Da)	206±3	195±11	212±27	249±15	228±11
H/C_w	1.53±0.01	1.53±0.01	1.48±0.23	1.47±0.22	1.76±0.2
O/C_w	0.41±0.02	0.42±0.03	0.36±0.02	0.42±0.04	0.67±0.03
DBE_w	3.65±0.07	3.40±0.31	4.43±1.51	4.51±1.29	3.51±0.32
DBE/C_w	0.36±0.01	0.35±0.00	0.43±0.11	0.37±0.12	0.38±0.09
AI_w	0.13±0.01	0.12±0.00	0.22±0.10	0.09±0.05	0.13±0.05

Site 120 (n = 1)						
Number of formulas	645	392	1145	88	36
Percent of formulas (%)		610.6	187.8	13.614	5.66
Molecular weight (Da)	280	28673	212346	271	396
H/C_w	1.41	1.467	0.996	1.51	1.15
O/C_w	0.34	0.32	0.485	0.50	0.44
DBE_w	5.6382	5.4410	6.409.84	5.19	11.97
DBE/C_w	0.389	0.34	0.7169	0.35	0.59
AI_w	0.145	0.0940	0.534	0.13	0.26

563
564

565   The mass spectra plots constructed from individual samples showing integrated

566   composition of U, R, S, and site 120 samples along with the corresponding number

567   contributions from different formula categories are shown in Fig. 4. Overall, the

568   assigned formulas were mainly in the mass range of 100 to 450 Da for both ESI+ and

569   ESI-, while there were more compounds with masses lower than 100 in the ESI+ mode.

570   The relative intensities of MS features contributed by compounds in different mass

571   ranges extract more information from the mass spectra, as shown in Fig. 5. In ESI-

572   mode, the ion intensity was most abundant in the mass range of 200 to 250 Da for U

573   samples, 250 to 300 Da for R and site 120 samples, and 150 to 200 Da for S samples,

574   indicating different chemical constituents for samples from different groups. The

575   variations in terms of relative intensities for CHO- compounds were like those of all

576   species detected in ESI-. For CHON-, formulas with mass of 150 to 200 Da were

577   abundant in S samples, while other groups were dominant by formulas in the range of

578   100 to 150 Da. Sample from site 120 showed higher fractions of formulas with masses

579   larger than 300 Da, especially for CHONS- compounds. The distributions of all

580   detected compounds showed higher contributions from mass range of 300 to 350 Da in

581   ESI+ compared to ESI-. Although detection of CH compounds in ESI is uncommon,

582   some of them appear detectable in the ESI+ mode, most were associated with aromatic

583   species smaller than 150 Da (DBE$\geq$4). Furthermore, the CHONS+ species showed

584   higher masses than CHONS-, except for the sample from site 120.
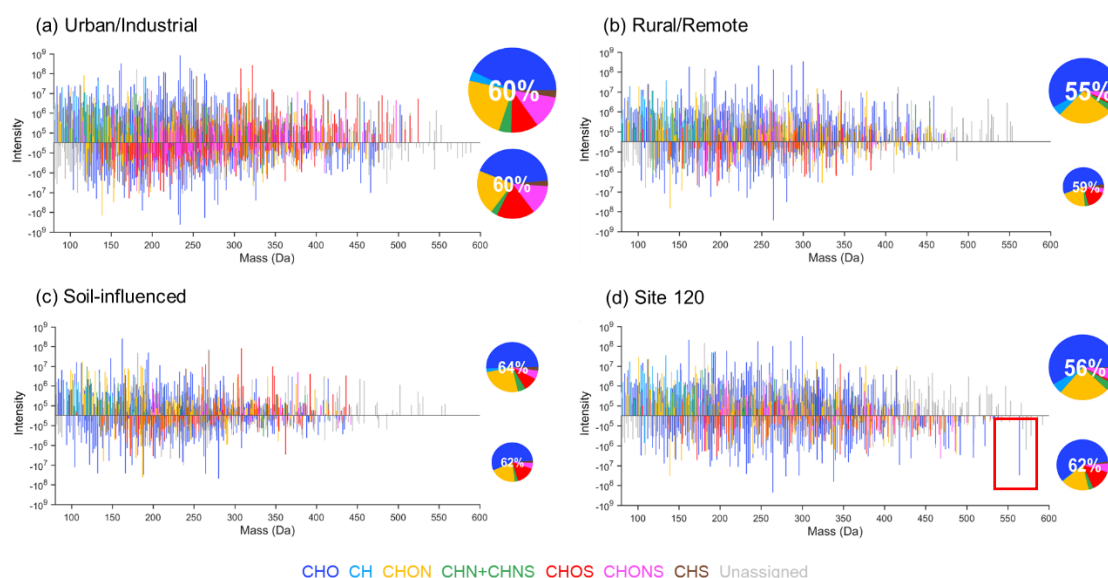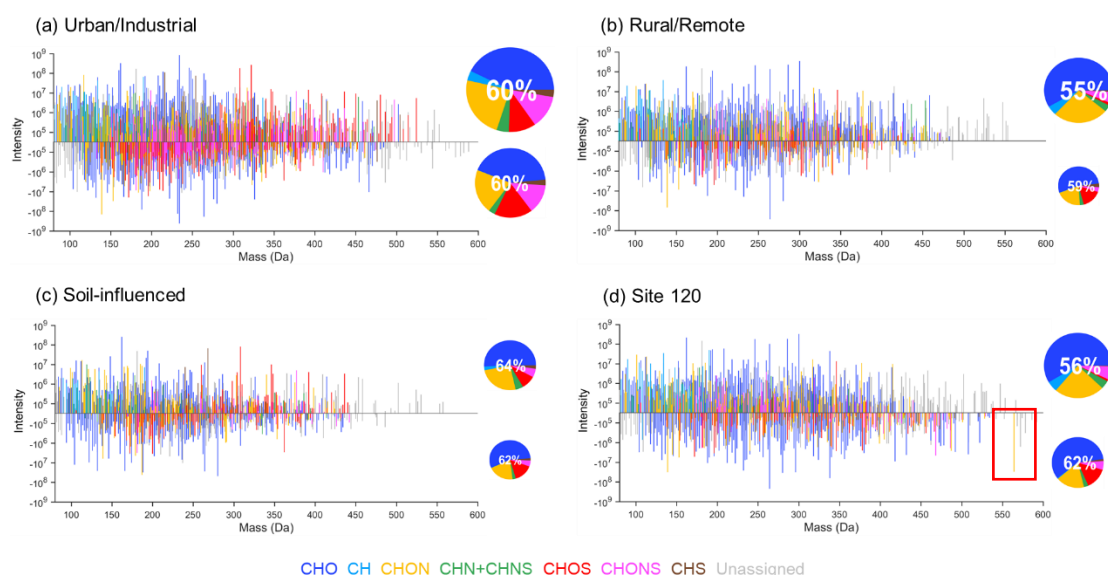
Figure 4. The reconstructed mass spectra of representative samples for four groups of sites: (a) site 114, (b) site 123, (c) site 104, (d) site 120. The data measured by ESI+/- are plotted as positive/negative intensities, respectively. The pie charts show the number contributions from different formula categories indicated by different colors, and the sizes of pie charts are proportional to the total numbers of assigned formulas detected in each sample by ESI+/-. The percentages present the ratios of assigned formula to total MS peaks. Unassigned peaks were converted into neutral mass by assuming that they were protonated in ESI+ and deprotonated in ESI-.
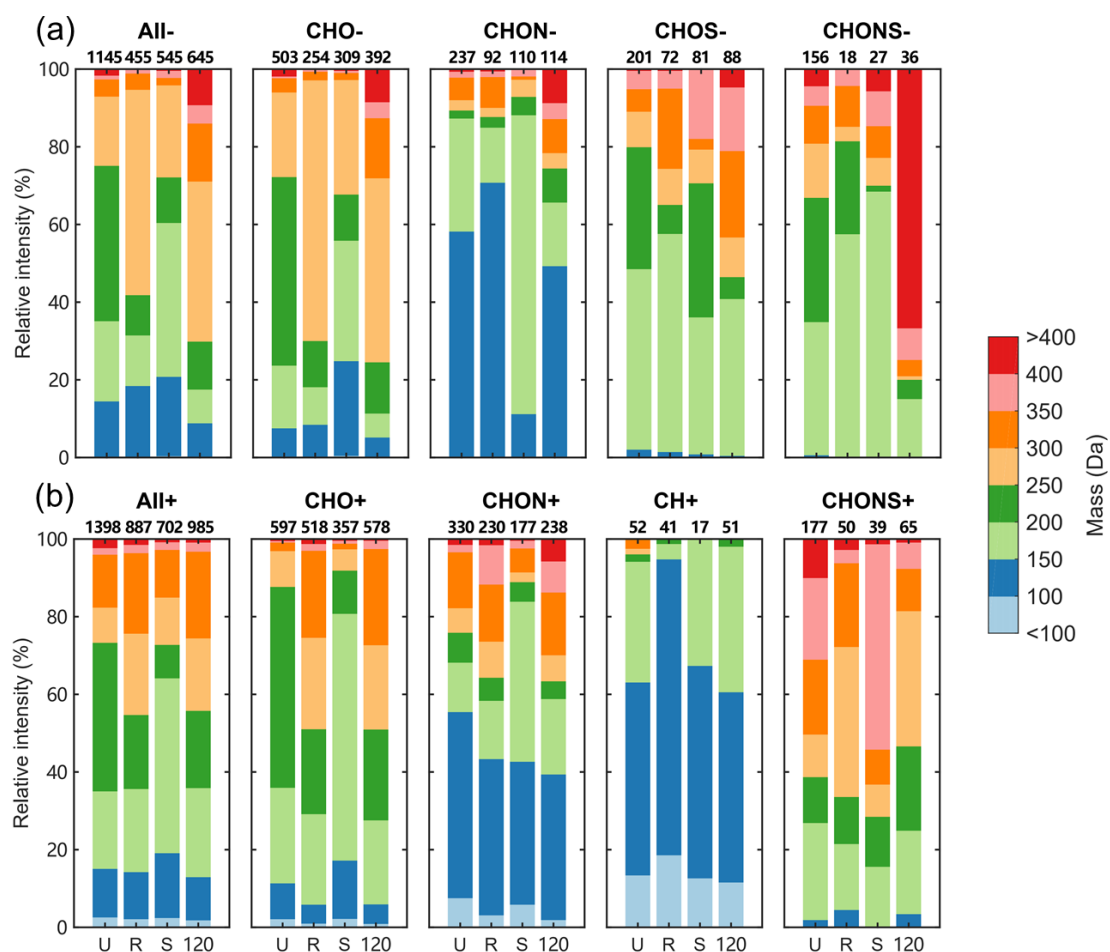
Figure 5. The distributions for relative intensities of compounds in different mass ranges in (a) ESI-and (b) ESI+. The numbers on the top of bars indicate the number of assigned peaks in different formula categories of each sample.

In ESI+ mode, CHO+ and CHON+ were the main components in all samples, accounting for 35% to 61% and 20% to 28% of total formulas, respectively (Table 1). The U samples showed the lowest CHO+ abundance (mean: 42%±5%) while the sample from site 120 had the highest value (59%). The fractions of CHON+ species in our samples were significantly lower than those of the aged firn/ice samples from the TP (~40%) (Feng et al., 2016, 2018, 2020;Spencer et al., 2014) which is mainly attributed to less microbial activities in our samples in which WSOC showed high bioavailability; but were comparable with the WSOC samples from those of fresh snow

 (Feng et al., 2018, 2020) in which the major source of WSOC is aerosol wet/dry

deposition. These results indicate that WSOC from the snowpack in northern Xinjiang

was more likely from atmospheric aerosol depositions rather than from autochthonous

sources. There were much higher contributions of S-containing compounds in the U

samples, e.g., CHOS+ (11%), CHONS+ (12%), and CHS+ (4%), which were less

abundant in other samples. These species showed low oxidation level (mean O/C_w: 0.07

for CHOS+), high unsaturation degree and aromaticity (mean DBE_w: 10.1 and 8.7;

mean AI_w: 0.42 and 0.48 for CHOS+ and CHS+, respectively), suggesting that they

might be reduced S-containing species with aromatic structures from incomplete fossil

fuel combustion (Mead et al., 2015; Wang et al., 2017a).

The abundance of CHO- was highest in ESI- with a range of 41% to 61%. The U

samples and the site 120 sample showed the lowest (mean: 47%±4%) and highest (61%)

fractions of CHO-, respectively. The CHON- and CHOS- compounds account for

roughly equal contributions with ranges of 16% to 27% and 14% to 22%, respectively.

The detected CHOS compounds were more abundant in ESI- than those in ESI+.

Furthermore, CHOS- compounds shows much higher oxidation level and lower

unsaturation degrees than CHOS+ (mean O/C_w: 0.55 and 0.08; mean DBE: 8.3 and 3.2

for CHOS- and CHOS+, respectively). These results are consistent with previous

ambient aerosol characterization studies (Lin et al., 2012; Wang et al., 2017a, 2018), but

the S-containing species were not abundantly detected in the glacier samples (Feng et

al., 2016; Spencer et al., 2014), indicating stronger influence from anthropogenic

aerosols to WSOC in Xinjiang seasonal snow than those from remote areas.

The bulk molecular characteristics of compounds detected in ESI+ and ESI- are

summarized in Tables 1 and 2, respectively. The MW_w of all compounds detected in

ESI+ mode was 231±9 Da, 229±10 Da, 218±15 Da, and 234 Da for U, R, S, and site

632   120 samples, respectively. These values are comparable with the MW_w of urban aerosols

633   (~225 to 265 Da) (Lin et al., 2012;Wang et al., 2018), but significantly lower than those

634   of glacier samples (~360 Da to 420 Da), suggesting different compositions between

635   WSOC in seasonal snow of our study and from the literature reported glacier samples.

636   *DBE* is used to infer the unsaturation degree of individual species (McLafferty et al.,

637   1993) and *AI* is a more direct metric of their aromaticity (Koch and Dittmar, 2006,

638   2016). The U samples showed higher DBE_w and AI_w values than the other groups of

639   samples mainly due to high fractions of S-containing compounds in ESI+ mode (Table

640   1). ~~In~~ As for ESI- mode, the MW_w of the site 120 sample was higher than the other

641   samples (280 Da vs. ~200 – 220 Da). Of note, the average MW_w of CHO~~N~~- and

642   CHONS- compounds in the site 120 sample were 286~~316~~ Da and 396 Da, respectively,

643   which were approximately ~~100~~ 70 Da and 150 Da higher than those from the other

644   groups of samples. Accordingly, the DBE_w of all formulas detected in the site 120

645   sample was the highest (5.8), the values for CHO~~N~~- and CHONS- were ~~9.8~~5.4 and 12.0,

646   respectively, which were approximately ~~2~~ 1.5 and 3 times higher than in the other

647   samples. These results indicate very unusual sources of WSOC in the site 120 sample.

648   Additionally, the molecular characteristics of formulas detected in ESI- and ESI+ are

649   different, e.g., higher average DBE_w and AI_w values of R samples for ESI- data (Tables

650   1 and 2). This results from the differences of ionization mechanisms between positive

651   and negative modes. ESI+ is sensitive to protonatable compounds with basic functional

652   groups, while acidic species are easily deprotonated and detected in ESI- mode (Cech

653   and Enke, 2001). Therefore, using both positive and negative ESI modes provide a more

654   complete molecular characterization of WSOC.

655

656

3.3.2 Chemical species in snow WSOC

The Van Krevelen (VK) diagram is a frequently used graphical method, which plots the H/C ratios against the O/C ratios in molecular formulas, to qualitatively determine the major chemical species in complex organic mixtures and to explore their potential reaction pathways (Kim et al., 2003). The VK diagrams of four representative samples detected in ESI+ and ESI- modes are shown in Fig. 6. The VK space in this study was separated into seven regions according to previous studies (Feng et al., 2016;Ohno et al., 2010): (1) lipids-like (O/C = 0−0.3, H/C = 1.5−2.0), (2) aliphatic/proteins-like (O/C = 0.3−0.67, H/C = 1.5−2.2), (3) carbohydrates-like (O/C=0.67−1.2; H/C=1.5−2.4), (4) unsaturated hydrocarbons (O/C = 0−0.1, H/C =0.7−1.5), (5) lignins/carboxylic-rich alicyclic molecules (CRAMs)-like (O/C = 0.1−0.67, H/C = 0.7−1.5), (6) tannins-like (O/C = 0.67−1.2, H/C = 0.5−1.5), and (7) condensed aromatics (O/C = 0−0.67, H/C = 0.2−0.7). In ESI+, the U samples showed the lowest O/C ratios (mean: 0.19±0.04) and H/C ratios (mean: 1.51±0.05) among four groups (Table 1), which indicate low oxygenation and high unsaturation degree of WSOC from U samples, likely ~~indicating~~suggesting their primary emission sources (Kroll et al., 2011). Consequently, the unsaturated hydrocarbons were most abundant among seven classes of species (mean: 39±15%, Table 3), most of which were CHOS+ compounds (Fig. S7), then followed by lignins/CRAMs-like species (mean: 25±11%). These results, again, supports our assumption that anthropogenic pollution is a major source of snow organics in the U region. The R samples exhibited the highest fraction of aliphatic/proteins-like species among four groups (mean: 57%±4%,). This type of species is widely distributed in natural dissolved organic matter detected in terrestrial water systems (Lu et al., 2015a), glaciers and polar ice sheets (Antony et al., 2014;Feng et al., 2016), aerosols (Ning et al., 2019;Wu et al., 2019a;Xie et al., 2020), and cloud

water (Bianco et al., 2018). The aliphatic/proteins-like species ~~are~~ is commonly regarded as a marker of biological-related sources, such as in-situ microbial activities (Antony et al., 2017) and primary bioaerosols (e.g., plant debris, fungal spores, and pollen) (Xie et al., 2020). The high contribution of aliphatic/proteins-like species in R samples is consistent with the results of our EEM-PARAFAC analysis, which showed that PRLIS fluorophore is the most abundant. The U samples and the site 120 sample showed high contributions of lignins/CRAMs-like species, but their sources might be different. The lignins/CRAMs-like species are commonly attributed to terrestrial-sourced, vascular plant-derived material (Antony et al., 2014), biomolecules with similar structures to sterols and hopanoids (Hertkorn et al., 2006), or secondary organic aerosols from biomass burning (Xie et al., 2020). These compounds in U samples were more likely from combustion of biomass materials, but those in the site 120 sample might be from biogenetic sources. In addition, ~~T~~the S samples showed higher contributions of unsaturated hydrocarbons (mean: 19%±14%~~,~~) than the R samples and the site 120 sample (mean: 11%±2% and 10%, respectively)~~., which were~~This result is mainly due to the CHOS+ compounds detected in the site 104 sample from R group (Fig. 6g)~~, which showed~~indicating some influence by anthropogenic pollution at this site.

701
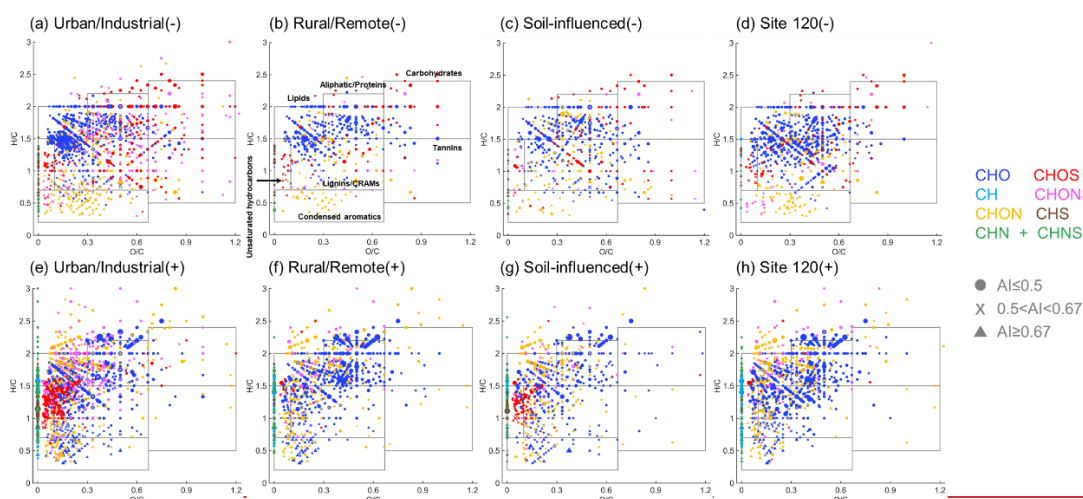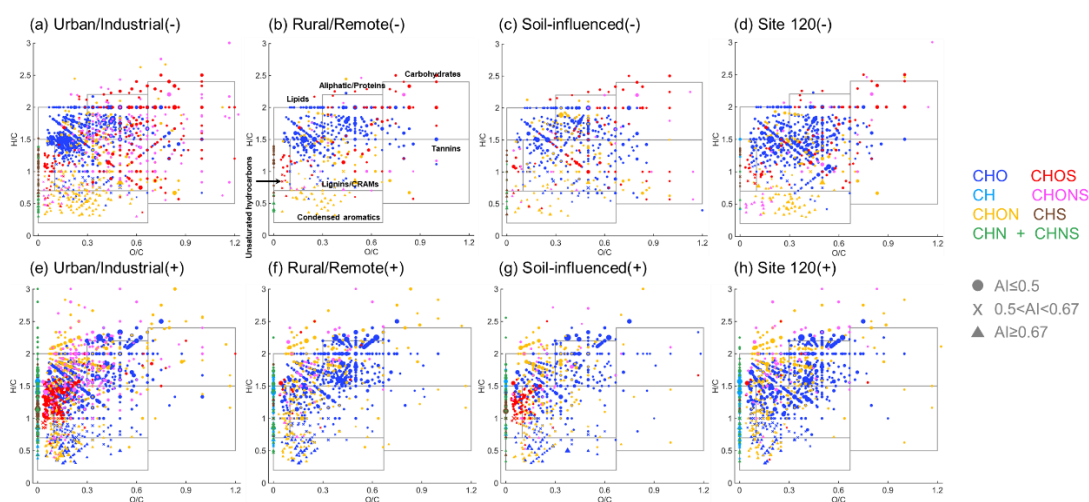
702 **Figure 6.** Van Krevelen diagrams of representative sample for each subgroup in (a-d) ESI- and (e-

703 h) ESI+. The boxes indicate the different classes of chemical species. Different formula categories

704 are color coded. Dots, crosses, and triangles represent non-aromatic (AI≤0.5), aromatic

705 (0.5<AI<0.67), and condensed aromatic compounds (AI≥0.67) (Koch and Dittmar, 2006),

706 respectively. The sizes of the symbols are proportional to the intensities.

707

708

Table 3. The relative abundance of different classes of molecular species in each group of sites.

		%Lipids-like	%Aliphatic/ protein-like	%Carbohydrates-like	%Unsaturated hydrocarbons	%Lignins/ CRAMs-like	%Tannins-like	%Condensed aromatics
U Urban/ Industrial (n = 14)	ESI+	18.2±9.1	154.6±121.7	0.2±0.1	3938.8±15.3	25.3±110.9	0	32.9±32.5
	ESI-	110.8±132.6	24.3±6.7	43.6±1.0	1.1±0.4	56.3±124.6	32.5±1.2	1.4±0.4
R Rural/Remote (n = 10)	ESI+	12.2±4.0	57.1±43.7	0.7±0.2	11.3±2.2	143.5±32.8	0.1	5.1±5.4
	ESI-	109.9±76.9	27.0±8.0	54.6±10.8	2.4±21.5	50.4±16.2	32.6±1.1	3.4±3.1
S Soil-influenced (n = 3)	ESI+	154.7±2.4	476.6±221.9	0.5±0.1	198.7±14.3	143.8±54.6	0.1	65.7±1.3
	ESI-	98.8±54.9	41.1±10.7	5.2±10.8	1.4±0.1	39.0±5.4	32.8±21.7	21.7±0.1
Site 120 (n = 1)	ESI+	14.2	52.2	0.4	10.1	22.8	0.1	1.3
	ESI-	65.8	13.0	2.1	2.0	754.5	0.8	21.7

709

710

711   The relative abundances of seven chemical species to four major formula categories

712   are shown in Fig. S7. Aliphatic/proteins-like species dominated the CHO+ compounds

713   in the R and the site 120 samples, while lignins/CRAMs-like species were most

714   abundant in the U sample. The contribution of condensed aromatics to CHO+ in the S

715   sample was high, which might be from soil-derived humic acids (DiDonato et al.,

716   2016;Ikeya et al., 2015). Lipids-like species were highly enriched in CHON+, except

717   for the U samples, in which significantly higher contributions from condensed

718   aromatics were observed. The condensed aromatics have typical AI values > 0.67 and

719   low O/C ratios which might be indicative of nitrated polycyclic aromatic hydrocarbons

720   (niro-PAHs) (Bandowe and Meusel, 2017) or N-heterocyclic aromatics (Bandowe et al.,

721   2016) from combustion sources. The CHOS+ compounds have mostly unsaturated

722   hydrocarbons characteristics in representative U and S samples as discussed above but

723   were rarely detected in the R and site 120 samples. The CHONS+ did not show distinct

724   variations among investigated samples, but higher fraction of aliphatic/proteins-like

725   species in the S sample was observed.

726   As for ESI-, the *O/C* (mean: 0.41±0.02) and *H/C* (mean: 1.53±0.01) ratios were

727   highest for species identified in the S samples, reflecting their higher oxygenation and

728   saturation levels. These values are similar to those of soil water extracted organic matter

729   (Ohno et al., 2010). This future is consistent with the results of EEM-PARAFAC, which

730   showed that highly-oxygenated HULIS-1 dominates in S samples. Lignins/CRAMs-

731   like species detected in ESI- dominated the VK space rather than aliphatic/proteins-like

732   compounds detected in ESI+. The relative contributions of seven chemical classes did

733   not change much between U and R samples (Table 3). In S samples, lower fraction of

734   lignins/CRAMs-like species was found. Compared to the water extracted organic

735   matter from pure soil sample (Ohno et al., 2010), our S samples showed similar

percentage of lignins/CRAMs-like species (39% vs. 44%). An extremely high contribution of lignins/CRAMs-like species (74.5%) was observed for the site 120 sample, strongly suggesting influence from biogenetic materials. As for the relative abundances in major formula categories, CHO- and CHON- were dominated by lignins/CRAMs-like species, except CHON- of the S sample, which exhibited highest fraction of aliphatic/proteins-like species. This highest CHON- fraction mainly resulted from a single compound with disproportionally high ion abundance, i.e., $C_9H_{17}O_3N$, which might be tentatively assigned as amino acid and led to a high fraction of aliphatic/proteins-like compounds in S samples (mean: 41%±1%). Amino acids are widely distributed in soil and are important organic nitrogen sources of soil microorganisms and plants (Geisseler et al., 2010). Moreover, biomass burning is also a significant source of atmospheric amino acids (Laskin et al., 2009;Lin et al., 2012). Therefore, either deposition of blowing soil or biomass burning aerosols may be responsible for the appearance of this high-abundance amino acid species in the S sample. As for CHOS- and CHONS-, lignins/CRAMs-like and carbohydrates-like species accounted for large portions of their total intensity. Only a few CHONS- compounds are apportioned as lignins/CRAMs-like species for the S sample, they are attributed mostly to carbohydrates-like species than anything else. One interesting note is that the contribution of condensed aromatics in the site 120 sample is highest among all samples. Specifically, there are some unique CHONS- compounds within the region of condensed aromatics, e.g., $C_{29}H_{14}O_4N_2S$ (DBE=24, AI=0.77) and $C_{26}H_{14}O_5N_2S$ (DBE=21, AI=0.72), which have high MW>400 Da. They may contain structure of anthraquinones, which are widely distributed in nature plants (Duval et al., 2016).

To further illustrate the differences of chemical compositions and structures among four groups of the investigated samples, plots of DBE versus C+N atomic number are

shown in Fig. 7. The numbers of unique formulas in the U sample were highest both in ESI+ and ESI- with values of 578 and 618 (Fig. S8), respectively, which accounted for 44% and 54% of total assigned species in each of the modes. These values were lowest for the R sample, with only 17% (145) and 11% (51) in ESI+ and ESI-, respectively. These results reflect very high chemical complexity of WSOC from U samples. The DBE plots of Fig. 7 are shown along with the reference lines depicting DBE values characteristic of (a) linear polyenes (C_xH_{x+2}, DBE = 0.5 × C) (Cain et al., 2014); (b) cata-condensed PAHs (DBE = 0.75 × C − 0.5) (Siegmann and Sattler, 2000); (c) fullerene-like hydrocarbons (DBE = 0.9 × C) (Lobodin et al., 2012). Because efficient absorption of visible light by organic molecules requires conjugated group of bonds extended across a significant part of the molecule, the compounds with the *DBE/C* greater than that of linear polyenes might be potential chromophores (Lin et al., 2018). The DBE values of CHON and CHONS compounds shift 1−5 units to the right as the sum-total number of carbon and nitrogen atoms are accounted for. In ESI-, 266 formulas of the U sample were in the "BrC domain" region, which was much higher than the other samples (26, 106, and 115 for the R, S, and site 120 sample, respectively). Most of them are CHON-, CHOS- and CHONS- compounds, accounting for 74% of the total formulas assigned in the U sample. Their C numbers and DBE values were mainly in the ranges of 4-16 and 4-10, respectively. For the S and site 120 samples, CHO- and CHON- were abundant in the "BrC domain" region (70% and 62% for the S and site 120 samples, respectively). The frequency distributions of C numbers and DBE were similar between the U and S samples, but WSOC components in the S samples showed higher *O/C* ratios for CHO- compounds (Fig. S9), again consistent with the soil organic matter (Ohno et al., 2010). However, the observations are quite different for the site 120 sample, where C numbers and DBE values gathered in broader ranges of 11-26 and 10-

786 20, respectively, with higher medians. In addition, a few of the CHON- and CHONS-

787 compounds with DBE higher than 17 were detected. These CHONS- formulas have

788 been identified as plant-related organics as discussed above. Similarly, the highly

789 unsaturated CHON- compounds, e.g., $C_{25}H_{13}O_8N$ (DBE=20, AI=0.69), $C_{26}H_{15}O_8N$

790 (DBE=20, AI=0.65), and $C_{26}H_{15}O_9N$ (DBE=20, AI=0.63), showed high MW>400 Da,

791 and they may also be tentatively assigned as anthraquinone derivatives. All these unique

792 compounds suggested that the biogenic organics from plants are major sources of

793 WSOC from the site 120 sample. In ESI+, the numbers of formulas within "BrC domain"

794 were 216, 43, 103, and 64 for the U, R, S, and site 120 samples, respectively. These

795 potential BrC species were largely attributed to CHO+ and CHON+ compounds (54%-

796 75%), whereas the S-containing compounds (34%) were substantial in the U sample.

797 Although the U samples showed the highest number of unique "BrC" molecules,

798 their bulk *MAC* values are lower than those measured for the S and site 120 samples.

799 Observation of the lower *MAC* values in the U samples is consistent with HRMS

800 characterization results showing that the high-intensity WSOC compounds are out of

801 the "BrC domain" region as shown in Fig. 7.

802

803
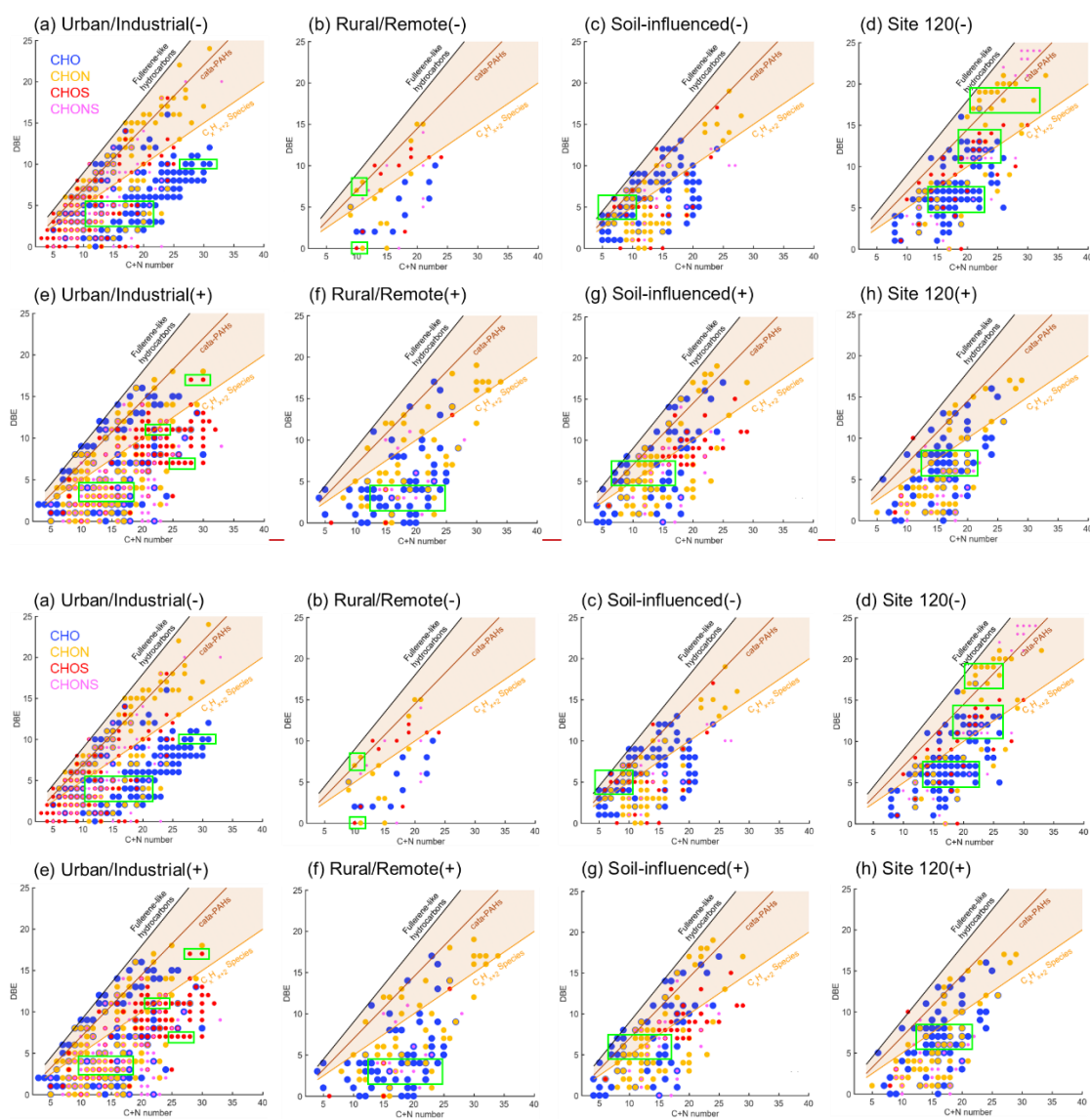
Figure 7. DBE vs. C+N number for unique molecules in representative samples from different groups. (a-d) ESI- and (e-h) ESI+. The reference lines indicate linear polyenes (C_xH_{x+2}, DBE = 0.5 × C), cata-condensed PAHs (DBE = 0.75 × C − 0.5), and fullerene-like hydrocarbons (DBE = 0.9 × C). Markers in the shaded area are potential BrC chromophores. The green boxes denote the high-intensity compounds. Four major formula categories are shown in different colors and sizes to avoid overlapping.

3.4 The radiative forcing by BrC attributed to WSOC in the snowpack

Inherent to the complexity of WSOC material and variability of its BrC optical properties, quantitative estimates of its *RF* in snowpack remain insufficiently studied.

Yan et al. (2016) calculated the BrC-induced RF at LHG glacier from the TP region, which was 0.43 W m^{-2} and accounted for 10% of RF due to BC. Most recently, Beres et al. (2020) described the spectral albedo and RF after artificial deposition of BrC aerosol proxies from peat burning onto ambient snow surface. They showed that the instantaneous RF efficiency due to total deposited aerosol was 1.23 W m^{-2} per ppm of the deposited mass. However, in the real world, BrC concentrations may not be that high as in the proxy experiments. Also, daily averaged values of RF are more important for the climate research. Here we contribute to this line of work by calculating the averaged-daily RF due to BC and BrC ($RF_{BC, BrC}$) deposits in snow based on the bulk characterization measurements over the samples of our study.

Figure 8 shows the snow spectral albedo (α_λ) simulated for four different scenarios, comparing albedo changes of the snowpack containing levels of BC and WSOC measured in the samples. Because most of the snowpack was shallow during the campaign, the albedo of pure snow was influenced by the effects of dark ground surface (albedo assumed to be 0.2) underlaying at the snow depth specific to each of the sites, as shown in Fig. 8. The average values of $\Delta\alpha$ and RF due to BC and BrC at different spectral ranges are summarized in Table 4. As expected, BC have strong broadband impact on the snow albedo and corresponding RF effects. Specifically, U and S samples with high BC mass loadings (mean: 707 and 440 ng g^{-1}, respectively) show albedo reduction ($\Delta\alpha_{BC}$) by 0.034 and 0.037 over broad 300-1500 nm wavelength range, respectively, and the corresponding RF_{BC} estimates are as high as 3.5 W m^{-2}. In addition, S and site 120 samples with higher WSOC concentrations (mean: 2082 and 7069 ng g^{-1}, respectively) show lower broadband albedo reduction ($\Delta\alpha_{BrC}$) of ~0.006 and the corresponding RF_{BrC} of ~0.6 W m^{-2}. Notably, because of the low BC and high WSOC mass loadings in the site 120 sample, its RF_{BrC} estimate is approximately 2 times higher

than RF_{BC}. For the other samples (U, R, and S), the RF_{BrC} is still significant with the average ratios of RF_{BrC}/RF_{BC} being at the level of 0.07-0.16. These results indicated that BrC have profound impact on the reduction of the snow albedo in Northern Xinjiang. As shown in Fig. 9, due to the stronger wavelength dependence of BrC absorption, the spectral albedo reduction by BrC increased sharply at shorter wavelengths (300-400 nm), where $\Delta\alpha_{BrC}$ can be as large as 29-65% of the $\Delta\alpha_{BC}$ (Table 4). Unlike graphitic-like components of BC, water-soluble part of BrC can trigger photochemical reactions in snow forming reactive oxygen species (Fede and Grannas, 2015;Grannas et al., 2014), catalyzing reaction chemistry and accelerating its kinetics at snow/ice-air interface (Grannas et al., 2014;Hullar et al., 2020). Overall, these results emphasize important role of WSOC and its BrC components on tempering solar radiation balance and modulating environmental chemistry of organics and their air-snow partitioning pertinent to mid-latitude seasonal snowpack.

 Table 4. Simulated broadband albedo reduction due to BC and BrC within different wavelength ranges and the ratios between those of BrC and BC. The BC- and BrC-

 induced average-daily radiative forcing is also shown.

| | Broadband albedo reduction | | | | | | Radiative forcing | |
	300-400 nm			300-1500 nm			BC (W m^{-2})	BrC (W m^{-2})
	BC	BrC	BrC/BC	BC	BrC	BrC/BC		
U Industrial/Urban (n = 14)	0.059±0.056	0.015±0.013	0.29±0.19	0.034±0.034	0.002±0.002	0.07±0.06	3.38±3.54	0.21±0.21
R Remote/Rural (n = 10)	0.010±0.006	0.003±0.001	0.39±0.16	0.005±0.003	0.0004±0.0002	0.09±0.05	0.53±0.34	0.04±0.03
S Soil-influenced (n = 3)	0.069±0.001	0.044±0.025	0.65±0.37	0.037±0.002	0.006±0.003	0.16±0.08	3.49±0.26	0.55±0.28
Site **120** (n = 1)	0.005	0.066	12.02	0.003	0.006	2.16	0.27	0.59

858
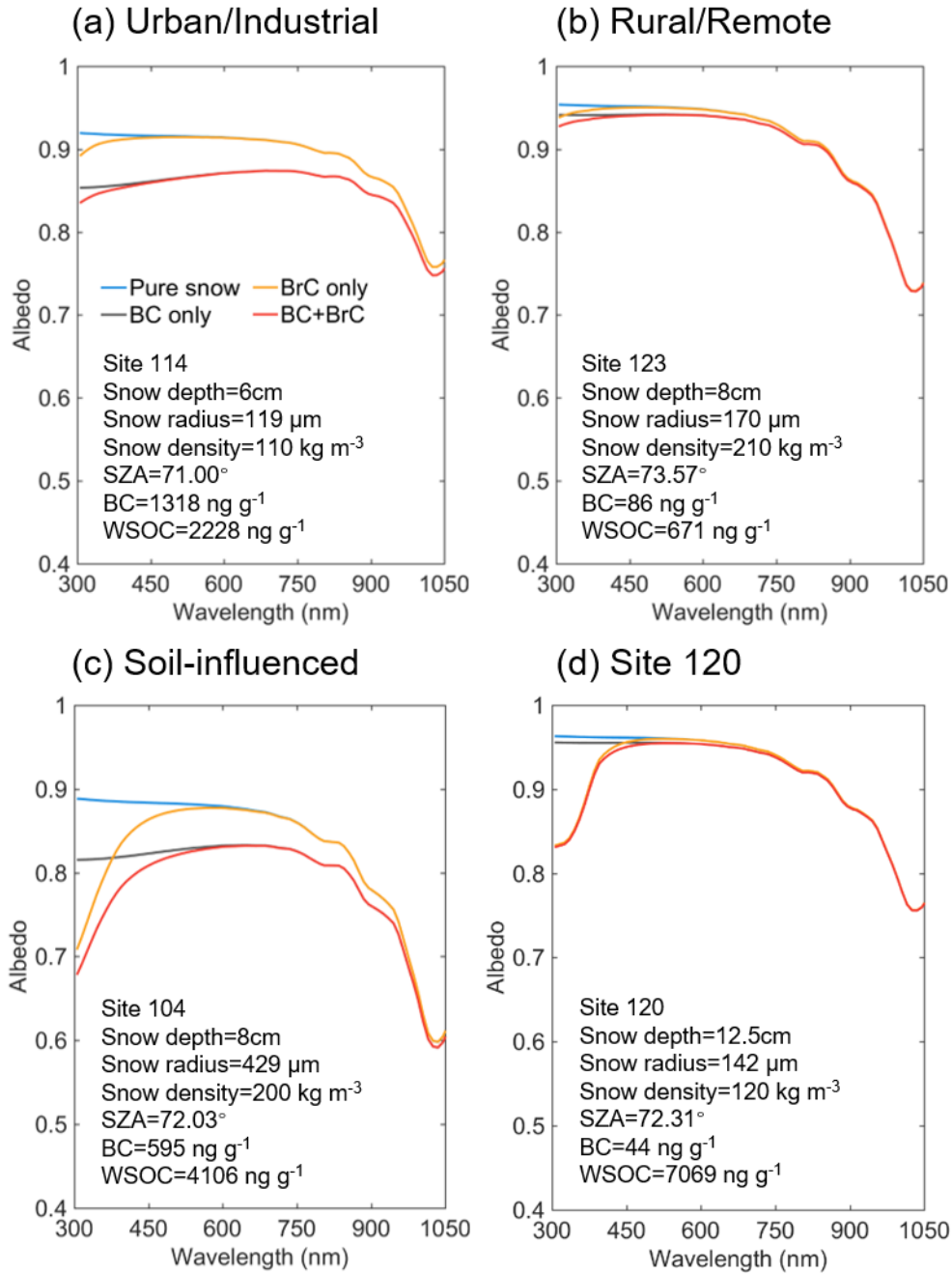
859 **Figure 8.** Simulated snow spectral albedo under different contamination scenarios for representative

860 samples from different groups. The blue, grey, yellow, and red lines exhibit the spectral albedos of

861 pure snow, BC- or BrC-contaminated snow, and snow polluted by both BC and BrC, respectively.

862 The input parameters of each site for SNICAR model are also shown.

863
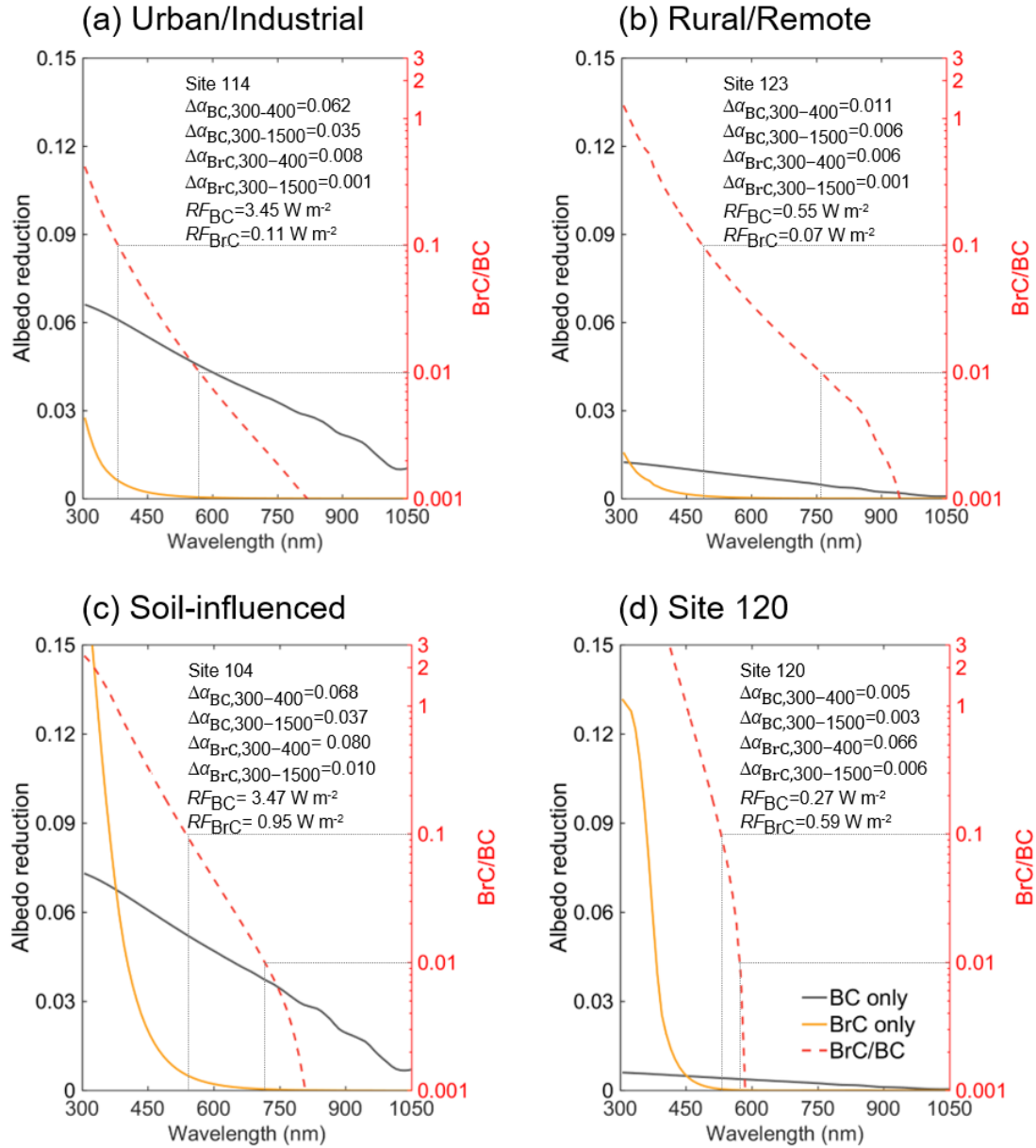
Figure 9. The albedo reduction spectra for representative samples from different groups. The grey and yellow lines show the albedo reductions due to BC or BrC, respectively. The red lines show the ratios of albedo reductions by BrC to those by BC. The $\Delta\alpha_{BC,BrC}$ and $RF_{BC,BrC}$ of each site are also shown.

4 Conclusions

The concentrations, optical properties, and molecular compositions of WSOC in seasonal snow collected from 28 sampling sites in Northern Xinjiang, northwestern China, were measured by multiple analytical techniques. The average concentrations of

874 WSOC were 1968 ± 953 ng g^{-1}, 885 ± 328 ng g^{-1}, 2082 ± 1438 ng g^{-1}, and 7069 ng g^{-1} for

875 U, R, S, and site 120 samples, respectively, reflecting large variability of WSOC mass

876 loadings among different groups of sites. These values were generally higher than those

877 reported previously for samples from high-altitude or high-latitude regions. Site 120

878 sample showed the highest MAC_{365} (0.95 m^2 g^{-1}) along with an unusual shape of

879 absorption spectrum, followed by samples from S (0.94 ± 0.31 m^2 g^{-1}), U (0.39 ± 0.11 m^2

880 g^{-1}), and R (0.38 ± 0.12 m^2 g^{-1}) sites. BrC components of our samples showed either

881 comparable or somewhat lower light-absorbing properties compared to previous reports

882 of polar or glacier snow, and were identified as W-BrC according to the optical-based

883 classification (Saleh, 2020).

884   The differences in bulk chemical composition among four groups of samples were

885 elucidated by EEM spectroscopy assisted with PARAFAC analysis. Terrestrial-sourced

886 HULIS-1 factor accounted for 49% of the total fluorescence in S samples, indicating

887 the significant contributions from soil organic material. HULIS-2 factor dominated the

888 fluorescence intensity of U samples (46%). The anthropogenic sources of HULIS-2

889 were inferred from significantly positive correlation with sulfate ions indicative

890 combustion related sources. PRLIS factor was abundant in R samples (48%), reflecting

891 a potential source of labile WSOC from microbial activities. The EEM map of site 120

892 showed a unique peak never found in any other samples, which might be from plant

893 organics.

894   HPLC-ESI-HRMS provided further information of molecular composition and

895 sources of WSOC. Total, 561 to 1487 and 339 to 1568 formulas were assigned in ESI+

896 and ESI- mass spectra, respectively. The mass distributions with respect to relative

897 intensity were highly variable among representative samples of different groups in both

898 ESI+ and ESI- modes, indicating different composition for each of the samples. CHO+

and CHON+ were the major components detected in ESI+ mode for all samples. CHOS+ compounds were highly enriched in U samples. These species had low oxidation degree, high unsaturation level and aromaticity, suggesting S-containing aromatic organics presumably related to heavy fossil fuels. In the ESI- detection mode, CHO- compounds were still dominated, but contribution from CHOS- was much higher, showing roughly equal abundance with CHON-. Through analysis of the VK diagrams, the major chemical species in snow WSOC were determined qualitatively. The unsaturated hydrocarbons were the most abundant species in U samples, most of them were CHOS+ from anthropogenic emissions. The R samples showed the highest contribution from aliphatic/proteins-like species, which is consistent with the results from EEM-PARAFAC analysis. The S samples showed high oxygenation and saturation degrees, and indicated the similar values of *O/C* and *H/C* ratios and percentage of lignins/CRAMs-like species compared to the soil organic matter (Ohno et al., 2010). An extremely high contribution of lignins/CRAMs-like species were found at the site 120 sample, suggesting the biogenetic sources of WSOC. Furthermore, a few unique CHON- and CHONS- compounds with DBE higher than 17 and MW larger than 400 Da were found at site 120. The most possible candidates for them were species with anthraquinone structures. Therefore, the special spectroscopic features of BrC from the site 120 sample was attributed to biogenic organics from plants.

The *RF* due to BrC in snow was reported, for the first time, based on the field data and model simulations. In general, the RF_{BrC} were at the levels of 0.04 to 0.59 W m^{-2} among different groups of sites and contributed to 7% to 16% of RF_{BC}. Therefore, we demonstrated the important influences of WSOC on the snow energy budget and potentially on triggering snow photochemistry. This study presents a comprehensively ~~overview~~chemical characterization —of WSOC and its BrC properties in collected

924 seasonal snow samples ~~of~~ from Northern Xinjiang, northwestern China, which helps to

925 better understand their characteristics, sources, and climate effects.

926

927 *Data availability.* Requests for all data in this study and any questions regarding the

928 data can be directed to Alexander Laskin (alaskin@purdue.edu) or Xin Wang

929 (wxin@lzu.edu.cn).

930

931 *Author contributions.* YZ, CW, AH, XN, and HW designed and conducted the lab

932 experiments. YZ processed the data with assist of CW and AH and wrote the paper. XW,

933 YZ, XN, JC, TS, WP, and HW designed and conducted the field campaign, collected

934 the snow samples, and discussed the results. AL and XW supervised this study. All co-

935 authors commented on the paper and improved it.

936

937 *Competing interests.* The authors declare that they have no conflict of interest.
938

939 *Acknowledgments.* Lanzhou University group acknowledges support from the National

940 Science Fund for Distinguished Young Scholars (42025102) and the National Natural

941 Science Foundation of China (41975157). Purdue group acknowledges support from

942 the Purdue Climate Change Research Center and the US Department of Energy's (DOE)

943 Atmospheric System Research program, Office of Biological and Environmental

944 Research (OBER), award DE-SC0018948. YZ acknowledges support from China

945 Scholarship Council.

946

References

Amoroso, A., Domine, F., Esposito, G., Morin, S., Savarino, J., Nardino, M., Montagnoli, M., Bonneville, J. M., Clement, J. C., Ianniello, A., and Beine, H. J.: Microorganisms in Dry Polar Snow Are Involved in the Exchanges of Reactive Nitrogen Species with the Atmosphere, Environ. Sci. Technol., 44, 714-719, 10.1021/es9027309, 2010.

Anastasio, C., and Robles, T.: Light absorption by soluble chemical species in Arctic and Antarctic snow, J. Geophys. Res. Atmos., 112, D24304, 10.1029/2007JD008695, 2007.

Andreae, M. O., and Gelencser, A.: Black carbon or brown carbon? The nature of light-absorbing carbonaceous aerosols, Atmos. Chem. Phys., 6, 3131-3148, 10.5194/acp-6-3131-2006, 2006.

Antony, R., Grannas, A. M., Willoughby, A. S., Sleighter, R. L., Thamban, M., and Hatcher, P. G.: Origin and Sources of Dissolved Organic Matter in Snow on the East Antarctic Ice Sheet, Environ. Sci. Technol., 48, 6151-6159, 10.1021/es405246a 2014.

Antony, R., Willoughby, A. S., Grannas, A. M., Catanzano, V., Sleighter, R. L., Thamban, M., Hatcher, P. G., and Nair, S.: Molecular Insights on Dissolved Organic Matter Transformation by Supraglacial Microbial Communities, Environ. Sci. Technol., 51, 4328-4337, 10.1021/acs.est.6b05780, 2017.

Bandowe, B. A., Meusel, H., Huang, R., Hoffmann, T., Cao, J., and Ho, K.: Azaarenes in fine particulate matter from the atmosphere of a Chinese megacity, Environ. Sci. Pollut. Res. Int., 23, 16025-16036, 10.1007/s11356-016-6740-z, 2016.

Bandowe, B. A. M., and Meusel, H.: Nitrated polycyclic aromatic hydrocarbons (nitro-PAHs) in the environment - A review, Sci. Total Environ., 581-582, 237-257, 10.1016/j.scitotenv.2016.12.115, 2017.

Bartels-Rausch, T., Brigante, M., Elshorbany, Y. F., Ammann, M., D'Anna, B., George, C., Stemmler, K., Ndour, M., and Kleffmann, J.: Humic acid in ice: Photo-enhanced conversion of nitrogen dioxide into nitrous acid, Atmos. Environ., 44, 5443-5450, 10.1016/j.atmosenv.2009.12.025, 2010.

Beine, H., Anastasio, C., Esposito, G., Patten, K., Wilkening, E., Domine, F., Voisin, D., Barret, M., Houdier, S., and Hall, S.: Soluble, light-absorbing species in snow at Barrow, Alaska, J. Geophys. Res. Atmos., 116, D00R05, 10.1029/2011jd016181, 2011.

Beres, N. D., Sengupta, D., Samburova, V., Khlystov, A. Y., and Moosmüller, H.: Deposition of brown carbon onto snow: changes in snow optical and radiative properties, Atmos. Chem. Phys., 20, 6095-6114, 10.5194/acp-20-6095-2020, 2020.

Bhatia, M. P., Das, S. B., Longnecker, K., Charette, M. A., and Kujawinski, E. B.: Molecular characterization of dissolved organic matter associated with the Greenland ice sheet, Geochim. Cosmochim. Acta, 74, 3768-3784, 10.1016/j.gca.2010.03.035, 2010.

Bianco, A., Deguillaume, L., Vaitilingom, M., Nicol, E., Baray, J. L., Chaumerliac, N., and Bridoux, M.: Molecular Characterization of Cloud Water Samples Collected at the Puy de Dome (France) by Fourier Transform Ion Cyclotron Resonance Mass Spectrometry, Environ. Sci. Technol., 52, 10275-10285, 10.1021/acs.est.8b01964, 2018.

Birdwell, J. E., and Valsaraj, K. T.: Characterization of dissolved organic matter in fogwater by excitation-emission matrix fluorescence spectroscopy, Atmos. Environ., 44, 3246-3253, 10.1016/j.atmosenv.2010.05.055, 2010.

Bond, T. C., and Bergstrom, R. W.: Light absorption by carbonaceous particles: An investigative review, Aerosol Sci. Technol., 40, 27-67, 10.1080/02786820500421521, 2006.

Bond, T. C., Doherty, S. J., Fahey, D. W., Forster, P. M., Berntsen, T., DeAngelo, B. J., Flanner, M. G., Ghan, S., Karcher, B., Koch, D., Kinne, S., Kondo, Y., Quinn, P. K., Sarofim, M. C., Schultz, M. G., Schulz, M., Venkataraman, C., Zhang, H., Zhang, S., Bellouin, N., Guttikunda, S. K., Hopke, P. K., Jacobson, M. Z., Kaiser, J. W., Klimont, Z., Lohmann, U., Schwarz, J. P., Shindell, D., Storelvmo, T., Warren, S. G., and Zender, C. S.: Bounding the role of black carbon in the climate system: A scientific assessment, J. Geophys. Res. Atmos., 118, 5380-5552, 10.1002/jgrd.50171, 2013.

Brutel-Vuilmet, C., Menegoz, M., and Krinner, G.: An analysis of present and future seasonal Northern Hemisphere land snow cover simulated by CMIP5 coupled climate models, The Cryosphere, 7, 67-80, 10.5194/tc-7-67-2013, 2013.

Cain, J., Laskin, A., Kholghy, M. R., Thomson, M. J., and Wang, H.: Molecular characterization of organic content of soot along the centerline of a coflow diffusion flame, Phys. Chem. Chem. Phys., 16, 25862-25875, 10.1039/c4cp03330b, 2014.

Cech, N. B., and Enke, C. G.: Practical implications of some recent studies in electrospray ionization fundamentals, Mass Spectrom. Rev., 20, 362-387, 10.1002/mas.10008, 2001.

Chen, Q., Mu, Z., Song, W., Wang, Y., Yang, Z., Zhang, L., and Zhang, Y. L.: Size-Resolved Characterization of the Chromophores in Atmospheric Particulate Matter From a Typical Coal-Burning City in China, J. Geophys. Res. Atmos., 124, 10546-10563, 10.1029/2019jd031149, 2019.

Chen, Q., Li, J., Hua, X., Jiang, X., Mu, Z., Wang, M., Wang, J., Shan, M., Yang, X., Fan, X., Song, J., Wang, Y., Guan, D., and Du, L.: Identification of species and sources of atmospheric chromophores by fluorescence excitation-emission matrix with parallel factor analysis, Sci. Total Environ., 718, 137322, 10.1016/j.scitotenv.2020.137322, 2020.

Chen, Q. C., Ikemori, F., and Mochida, M.: Light Absorption and Excitation-Emission Fluorescence of Urban Organic Aerosol Components and Their Relationship to Chemical Structure, Environ. Sci. Technol., 50, 10859-10868, 10.1021/acs.est.6b02541, 2016a.

Chen, Q. C., Miyazaki, Y., Kawamura, K., Matsumoto, K., Coburn, S., Volkamer, R., Iwamoto, Y., Kagami, S., Deng, Y. G., Ogawa, S., Ramasamy, S., Kato, S., Ida, A., Kajii, Y., and Mochida, M.: Characterization of Chromophoric Water-Soluble Organic Matter in Urban, Forest, and Marine Aerosols by HR-ToF-AMS Analysis and Excitation Emission Matrix Spectroscopy, Environ. Sci. Technol., 50, 10351-10360, 10.1021/acs.est.6b01643, 2016b.

Chen, Y., and Bond, T. C.: Light absorption by organic carbon from wood combustion, Atmos. Chem. Phys. , 10, 1773-1787, 10.5194/acp-10-1773-2010, 2010.

Coble, P. G.: Characterization of marine and terrestrial DOM in seawater using excitation emission matrix spectroscopy, Mar. Chem., 51, 325-346, 10.1016/0304-4203(95)00062-3, 1996.

Coble, P. G., Del Castillo, C. E., and Avril, B.: Distribution and optical properties of CDOM in the Arabian Sea during the 1995 Southwest Monsoon, Deep-Sea Res. Pt. II, 45, 2195-2223, 10.1016/S0967-0645(98)00068-X, 1998.

Cook, J. M., Hodson, A. J., Gardner, A. S., Flanner, M., Tedstone, A. J., Williamson, C., Irvine-Fynn, T. D. L., Nilsson, J., Bryant, R., and Tranter, M.: Quantifying

bioalbedo: a new physically based model and discussion of empirical methods for characterising biological influence on ice and snow albedo, Cryosphere, 11, 2611-2632, 10.5194/tc-11-2611-2017, 2017a.

Cook, J. M., Hodson, A. J., Taggart, A. J., Mernild, S. H., and Tranter, M.: A predictive model for the spectral "bioalbedo" of snow, J. Geophys. Res. Earth, 122, 434-454, 10.1002/2016JF003932, 2017b.

DiDonato, N., Chen, H., Waggoner, D., and Hatcher, P. G.: Potential origin and formation for molecular components of humic acids in soils, Geochim. Cosmochim. Acta 178, 210-222, 10.1016/j.gca.2016.01.013, 2016.

Doherty, S. J., Warren, S. G., Grenfell, T. C., Clarke, A. D., and Brandt, R. E.: Light-absorbing impurities in Arctic snow, Atmos. Chem. Phys., 10, 11647-11680, 10.5194/acp-10-11647-2010, 2010.

Duarte, R. M. B. O., Santos, E. B. H., Pio, C. A., and Duarte, A. C.: Comparison of structural features of water-soluble organic matter from atmospheric aerosols with those of aquatic humic substances, Atmos. Environ. , 41, 8100-8113, 10.1016/j.atmosenv.2007.06.034, 2007.

Duval, J., Pecher, V., Poujol, M., and Lesellier, E.: Research advances for the extraction, analysis and uses of anthraquinones: A review, Ind. Crops Prod., 94, 812-833, 10.1016/j.indcrop.2016.09.056, 2016.

Elliott, A., Mundy, C. J., Gosselin, M., Poulin, M., Campbell, K., and Wang, F.: Spring production of mycosporine-like amino acids and other UV-absorbing compounds in sea ice-associated algae communities in the Canadian Arctic, Mar. Ecol. Prog. Ser., 541, 91-104, 10.3354/meps11540, 2015.

Fede, A., and Grannas, A. M.: Photochemical Production of Singlet Oxygen from Dissolved Organic Matter in Ice, Environ. Sci. Technol., 49, 12808-12815, 10.1021/acs.est.5b03600, 2015.

Fellman, J. B., Hood, E., Raymond, P. A., Stubbins, A., and Spencer, R. G. M.: Spatial Variation in the Origin of Dissolved Organic Carbon in Snow on the Juneau Icefield, Southeast Alaska, Environ. Sci. Technol., 49, 11492-11499, 10.1021/acs.est.5b02685, 2015.

Feng, L., Xu, J. Z., Kang, S. C., Li, X. F., Li, Y., Jiang, B., and Shi, Q.: Chemical Composition of Microbe-Derived Dissolved Organic Matter in Cryoconite in Tibetan Plateau Glaciers: Insights from Fourier Transform Ion Cyclotron Resonance Mass Spectrometry Analysis, Environ. Sci. Technol., 50, 13215-13223, 10.1021/acs.est.6b03971, 2016.

Feng, L., An, Y., Xu, J., and Kang, S.: Characteristics and sources of dissolved organic matter in a glacier in the northern Tibetan Plateau: differences between different snow categories, Ann. Glaciol., 59, 31-40, 10.1017/aog.2018.20, 2018.

Feng, L., An, Y., Xu, J., Li, X., Jiang, B., and Liao, Y.: Biochemical evolution of dissolved organic matter during snow metamorphism across the ablation season for a glacier on the central Tibetan Plateau, Sci. Rep., 10, 6123, 10.1038/s41598-020-62851-w, 2020.

Flanner, M. G., Zender, C. S., Randerson, J. T., and Rasch, P. J.: Present-day climate forcing and response from black carbon in snow, J. Geophys. Res. Atmos., 112, D11202, 10.1029/2006jd008003, 2007.

Fu, P. Q., Kawamura, K., Chen, J., Qin, M. Y., Ren, L. J., Sun, Y. L., Wang, Z. F., Barrie, L. A., Tachibana, E., Ding, A. J., and Yamashita, Y.: Fluorescent water-soluble organic aerosols in the High Arctic atmosphere, Sci. Rep., 5, 9845, 10.1038/Srep09845, 2015.

Ganey, G. Q., Loso, M. G., Burgess, A. B., and Dial, R. J.: The role of microbes in

snowmelt and radiative forcing on an Alaskan icefield, Nat. Geosci., 10, 754-759, 10.1038/ngeo3027, 2017.

Geisseler, D., Horwath, W. R., Joergensen, R. G., and Ludwig, B.: Pathways of nitrogen utilization by soil microorganisms – A review, Soil Biol. Biochem., 42, 2058-2067, 10.1016/j.soilbio.2010.08.021, 2010.

Grannas, A. M., Jones, A. E., Dibb, J., Ammann, M., Anastasio, C., Beine, H. J., Bergin, M., Bottenheim, J., Boxe, C. S., Carver, G., Chen, G., Crawford, J. H., Domine, F., Frey, M. M., Guzman, M. I., Heard, D. E., Helmig, D., Hoffmann, M. R., Honrath, R. E., Huey, L. G., Hutterli, M., Jacobi, H. W., Klan, P., Lefer, B., McConnell, J., Plane, J., Sander, R., Savarino, J., Shepson, P. B., Simpson, W. R., Sodeau, J. R., von Glasow, R., Weller, R., Wolff, E. W., and Zhu, T.: An overview of snow photochemistry: evidence, mechanisms and impacts, Atmos. Chem. Phys., 7, 4329-4373, 10.5194/acp-7-4329-2007, 2007.

Grannas, A. M., Pagano, L. P., Pierce, B. C., Bobby, R., and Fede, A.: Role of dissolved organic matter in ice photochemistry, Environ. Sci. Technol., 48, 10725-10733, 10.1021/es5023834, 2014.

Hadley, O. L., and Kirchstetter, T. W.: Black-carbon reduction of snow albedo, Nat. Clim. Chang., 2, 437-440, 10.1038/Nclimate1433, 2012.

Hagler, G. S. W., Bergin, M. H., Smith, E. A., and Dibb, J. E.: A summer time series of particulate carbon in the air and snow at Summit, Greenland, J. Geophys. Res. Atmos., 112, D21309, 10.1029/2007jd008993, 2007a.

Hagler, G. S. W., Bergin, M. H., Smith, E. A., Dibb, J. E., Anderson, C., and Steig, E. J.: Particulate and water-soluble carbon measured in recent snow at Summit, Greenland, Geophys. Res. Lett., 34, 10.1029/2007GL030110, 2007b.

Hall, D. K., Riggs, G. A., and Salomonson, V. V.: Development of Methods for Mapping Global Snow Cover Using Moderate Resolution Imaging Spectroradiometer Data, Remote Sens. Environ., 54, 127-140, 10.1016/0034-4257(95)00137-P, 1995.

Handley, S. R., Clifford, D., and Donaldson, D. J.: Photochemical Loss of Nitric Acid on Organic Films: a Possible Recycling Mechanism for NOx, Environ. Sci. Technol., 41, 3898-3903, 10.1021/es062044z, 2007.

Hansen, J., and Nazarenko, L.: Soot climate forcing via snow and ice albedos, Proc. Nat. Acad. Sci. U.S.A., 101, 423-428, 10.1073/pnas.2237157100, 2004.

He, C. L., Li, Q. B., Liou, K. N., Takano, Y., Gu, Y., Qi, L., Mao, Y. H., and Leung, L. R.: Black carbon radiative forcing over the Tibetan Plateau, Geophys. Res. Lett., 41, 7806-7813, 10.1002/2014GL062191, 2014.

He, Z., Mao, J., Honeycutt, C. W., Ohno, T., Hunt, J. F., and Cade-Menun, B. J.: Characterization of plant-derived water extractable organic matter by multiple spectroscopic techniques, Biol. Fert. Soils, 45, 609-616, 10.1007/s00374-009-0369-8, 2009.

Hertkorn, N., Benner, R., Frommberger, M., Schmitt-Kopplin, P., Witt, M., Kaiser, K., Kettrup, A., and Hedges, J. I.: Characterization of a major refractory component of marine dissolved organic matter, Geochim. Cosmochim. Acta, 70, 2990-3010, 10.1016/j.gca.2006.03.021, 2006.

Hood, E., Fellman, J., Spencer, R. G. M., Hernes, P. J., Edwards, R., D'Amore, D., and Scott, D.: Glaciers as a source of ancient and labile organic matter to the marine environment, Nature, 462, 1044-1047, 10.1038/nature08580, 2009.

Hood, E., Battin, T. J., Fellman, J., O'Neel, S., and Spencer, R. G. M.: Storage and release of organic carbon from glaciers and ice sheets, Nat. Geosci., 8, 91-96, 10.1038/NGEO2331, 2015.

Huang, J. P., Fu, Q. A., Zhang, W., Wang, X., Zhang, R. D., Ye, H., and Warren, S. G.:

Dust And Black Carbon In Seasonal Snow across Northern China, Bull. Am. Meteorol. Soc., 92, 175-181, 10.1175/2010BAMS3064.1, 2011.

Hullar, T., Bononi, F. C., Chen, Z., Magadia, D., Palmer, O., Tran, T., Rocca, D., Andreussi, O., Donadio, D., and Anastasio, C.: Photodecay of guaiacol is faster in ice, and even more rapid on ice, than in aqueous solution, Environ. Sci.-Proc. Imp., 22, 1666-1677, 10.1039/d0em00242a, 2020.

Hunt, J. F., and Ohno, T.: Characterization of Fresh and Decomposed Dissolved Organic Matter Using Excitation−Emission Matrix Fluorescence Spectroscopy and Multiway Analysis, J. Agric. Food. Chem., 55, 2121-2128, 10.1021/jf063336m, 2007.

Ikeya, K., Sleighter, R. L., Hatcher, P. G., and Watanabe, A.: Characterization of the chemical composition of soil humic acids using Fourier transform ion cyclotron resonance mass spectrometry, Geochim. Cosmochim. Acta, 153, 169-182, 10.1016/j.gca.2015.01.002, 2015.

Jacobson, M. Z.: Climate response of fossil fuel and biofuel soot, accounting for soot's feedback to snow and sea ice albedo and emissivity, J. Geophys. Res. Atmos., 109, D21201, 10.1029/2004jd004945, 2004.

Jaffé, R., Cawley, K. M., and Yamashita, Y.: Applications of Excitation Emission Matrix Fluorescence with Parallel Factor Analysis (EEM-PARAFAC) in Assessing Environmental Dynamics of Natural Dissolved Organic Matter (DOM) in Aquatic Environments: A Review, in: Advances in the Physicochemical Characterization of Dissolved Organic Matter: Impact on Natural and Engineered Systems, ACS Symposium Series, 1160, American Chemical Society, 27-73, 2014.

Jin, Z. H., Charlock, T. P., Rutledge, K., Stamnes, K., and Wang, Y. J.: Analytical solution of radiative transfer in the coupled atmosphere-ocean system with a rough surface, Appl. Opt., 45, 7443-7455, 10.1364/AO.45.007443, 2006.

Jones, H. G.: The ecology of snow-covered systems: a brief overview of nutrient cycling and life in the cold, Hydrol. Processes, 13, 2135-2147, 10.1002/(SICI)1099-1085(199910)13:14/15<2135::AID-HYP862>3.0.CO;2-Y, 1999.

Kim, S., Kramer, R. W., and Hatcher, P. G.: Graphical method for analysis of ultrahigh-resolution broadband mass spectra of natural organic matter, the van Krevelen diagram, Anal. Chem., 75, 5336-5344, 10.1021/ac034415p, 2003.

Kirchstetter, T. W., Novakov, T., and Hobbs, P. V.: Evidence that the spectral dependence of light absorption by aerosols is affected by organic carbon, J. Geophys. Res. Atmos., 109, D21208, 10.1029/2004jd004999, 2004.

Kirillova, E. N., Andersson, A., Han, J., Lee, M., and Gustafsson, O.: Sources and light absorption of water-soluble organic carbon aerosols in the outflow from northern China, Atmos. Chem. Phys., 14, 1413-1422, 10.5194/acp-14-1413-2014, 2014.

Koch, B. P., and Dittmar, T.: From mass to structure: an aromaticity index for high-resolution mass data of natural organic matter, Rapid Commun. Mass Spectrom., 20, 926-932, 10.1002/rcm.2386, 2006.

Koch, B. P., and Dittmar, T.: From mass to structure: an aromaticity index for high-resolution mass data of natural organic matter, Rapid Commun. Mass Spectrom., 30, 250-250, 10.1002/rcm.7433, 2016.

Kothawala, D. N., Murphy, K. R., Stedmon, C. A., Weyhenmeyer, G. A., and Tranvik, L. J.: Inner filter correction of dissolved organic matter fluorescence, Limnol. Oceanogr.-Meth., 11, 616-630, 10.4319/lom.2013.11.616, 2013.

Kroll, J. H., Donahue, N. M., Jimenez, J. L., Kessler, S. H., Canagaratna, M. R., Wilson, K. R., Altieri, K. E., Mazzoleni, L. R., Wozniak, A. S., Bluhm, H., Mysak, E. R.,

Smith, J. D., Kolb, C. E., and Worsnop, D. R.: Carbon oxidation state as a metric for describing the chemistry of atmospheric organic aerosol, Nat. Chem., 3, 133-139, 10.1038/nchem.948, 2011.

Laskin, A., Smith, J. S., Laskin, J. J. E. s., and technology: Molecular characterization of nitrogen-containing organic compounds in biomass burning aerosols using high-resolution mass spectrometry, Environ. Sci. Technol., 43, 3764-3771, 10.1021/es803456n, 2009.

Laskin, A., Laskin, J., and Nizkorodov, S. A.: Chemistry of Atmospheric Brown Carbon, Chem. Rev., 115, 4335-4382, 10.1021/cr5006167, 2015.

Lawaetz, A. J., and Stedmon, C. A.: Fluorescence Intensity Calibration Using the Raman Scatter Peak of Water, Appl. Spectrosc., 63, 936-940, 10.1366/000370209788964548, 2009.

Legrand, M., Preunkert, S., Jourdain, B., Guilhermet, J., Fain, X., Alekhina, I., and Petit, J. R.: Water-soluble organic carbon in snow and ice deposited at Alpine, Greenland, and Antarctic sites: a critical review of available data and their atmospheric relevance, Clim. Past, 9, 2195-2211, 10.5194/cp-9-2195-2013, 2013.

Lin, P., Engling, G., and Yu, J. Z.: Humic-like substances in fresh emissions of rice straw burning and in ambient aerosols in the Pearl River Delta Region, China, Atmos. Chem. Phys., 10, 6487-6500, 10.5194/acp-10-6487-2010, 2010.

Lin, P., Rincon, A. G., Kalberer, M., and Yu, J. Z.: Elemental composition of HULIS in the Pearl River Delta Region, China: results inferred from positive and negative electrospray high resolution mass spectrometric data, Environ. Sci. Technol., 46, 7454-7462, 10.1021/es300285d, 2012.

Lin, P., Aiona, P. K., Li, Y., Shiraiwa, M., Laskin, J., Nizkorodov, S. A., and Laskin, A.: Molecular Characterization of Brown Carbon in Biomass Burning Aerosol Particles, Environ. Sci. Technol., 50, 11815-11824, 10.1021/acs.est.6b03024, 2016.

Lin, P., Fleming, L. T., Nizkorodov, S. A., Laskin, J., and Laskin, A.: Comprehensive Molecular Characterization of Atmospheric Brown Carbon by High Resolution Mass Spectrometry with Electrospray and Atmospheric Pressure Photoionization, Anal. Chem., 90, 12493-12502, 10.1021/acs.analchem.8b02177, 2018.

Liu, Y. Q., Yao, T. D., Jiao, N. Z., Kang, S. C., Xu, B. Q., Zeng, Y. H., Huang, S. J., and Liu, X. B.: Bacterial diversity in the snow over Tibetan Plateau Glaciers, Extremophiles, 13, 411-423, 10.1007/s00792-009-0227-5, 2009.

Lobodin, V. V., Marshall, A. G., and Hsu, C. S.: Compositional Space Boundaries for Organic Compounds, Anal. Chem., 84, 3410-3416, 10.1021/ac300244f, 2012.

Lu, Y., Li, X., Mesfioui, R., Bauer, J. E., Chambers, R. M., Canuel, E. A., and Hatcher, P. G.: Use of ESI-FTICR-MS to Characterize Dissolved Organic Matter in Headwater Streams Draining Forest-Dominated and Pasture-Dominated Watersheds, Plos One, 10, e0145639, 10.1371/journal.pone.0145639, 2015a.

Lu, Z., Streets, D. G., Winijkul, E., Yan, F., Chen, Y., Bond, T. C., Feng, Y., Dubey, M. K., Liu, S., Pinto, J. P., and Carmichael, G. R.: Light absorption properties and radiative effects of primary organic aerosol emissions, Environ. Sci. Technol., 49, 4868-4877, 10.1021/acs.est.5b00211, 2015b.

Lutz, S., Anesio, A. M., Villar, S. E. J., and Benning, L. G.: Variations of algal communities cause darkening of a Greenland glacier, FEMS Microbiol. Ecol., 89, 402-414, 10.1111/1574-6941.12351, 2014.

McLafferty, F. W., Tureček, F., and Turecek, F.: Interpretation of mass spectra, University science books, 1993.

McNeill, V. F., Grannas, A. M., Abbatt, J. P. D., Ammann, M., Ariya, P., Bartels-Rausch, T., Domine, F., Donaldson, D. J., Guzman, M. I., Heger, D., Kahan, T. F., Klan, P.,

Masclin, S., Toubin, C., and Voisin, D.: Organics in environmental ices: sources, chemistry, and impacts, Atmos. Chem. Phys., 12, 9653-9678, 10.5194/acp-12-9653-2012, 2012.

Mead, R. N., Felix, J. D., Avery, G. B., Kieber, R. J., Willey, J. D., and Podgorski, D. C.: Characterization of CHOS compounds in rainwater from continental and coastal storms by ultrahigh resolution mass spectrometry, Atmos. Environ., 105, 162-168, 10.1016/j.atmosenv.2015.01.057, 2015.

Mladenov, N., Alados-Arboledas, L., Olmo, F. J., Lyamani, H., Delgado, A., Molina, A., and Reche, I.: Applications of optical spectroscopy and stable isotope analyses to organic aerosol source discrimination in an urban area, Atmos. Environ., 45, 1960-1969, 10.1016/j.atmosenv.2011.01.029, 2011.

Mladenov, N., Williams, M. W., Schmidt, S. K., and Cawley, K.: Atmospheric deposition as a source of carbon and nutrients to an alpine catchment of the Colorado Rocky Mountains, Biogeosciences, 9, 3337-3355, 10.5194/bg-9-3337-2012, 2012.

Murphy, K. R., Stedmon, C. A., Waite, T. D., and Ruiz, G. M.: Distinguishing between terrestrial and autochthonous organic matter sources in marine environments using fluorescence spectroscopy, Mar. Chem., 108, 40-58, 10.1016/j.marchem.2007.10.003, 2008.

Murphy, K. R., Stedmon, C. A., Graeber, D., and Bro, R.: Fluorescence spectroscopy and multi-way techniques. PARAFAC, Anal. Methods, 5, 6557-6566, 10.1039/c3ay41160e, 2013.

Myers, O. D., Sumner, S. J., Li, S., Barnes, S., and Du, X.: One Step Forward for Reducing False Positive and False Negative Compound Identifications from Mass Spectrometry Metabolomics Data: New Algorithms for Constructing Extracted Ion Chromatograms and Detecting Chromatographic Peaks, Anal. Chem., 89, 8696-8703, 10.1021/acs.analchem.7b00947, 2017.

Ning, C., Gao, Y., Zhang, H., Yu, H., Wang, L., Geng, N., Cao, R., and Chen, J.: Molecular characterization of dissolved organic matters in winter atmospheric fine particulate matters (PM2.5) from a coastal city of northeast China, Sci. Total Environ., 689, 312-321, 10.1016/j.scitotenv.2019.06.418, 2019.

Niu, H. W., Kang, S. C., Lu, X. X., and Shi, X. F.: Distributions and light absorption property of water soluble organic carbon in a typical temperate glacier, southeastern Tibetan Plateau, Tellus B, 70, 10.1080/16000889.2018.1468705, 2018.

Nizkorodov, S. A., Laskin, J., and Laskin, A.: Molecular chemistry of organic aerosols through the application of high resolution mass spectrometry, Phys. Chem. Chem. Phys., 13, 3612-3629, 10.1039/c0cp02032j, 2011.

Noziere, B., Kalberer, M., Claeys, M., Allan, J., D'Anna, B., Decesari, S., Finessi, E., Glasius, M., Grgic, I., Hamilton, J. F., Hoffmann, T., Iinuma, Y., Jaoui, M., Kahnt, A., Kampf, C. J., Kourtchev, I., Maenhaut, W., Marsden, N., Saarikoski, S., Schnelle-Kreis, J., Surratt, J. D., Szidat, S., Szmigielski, R., and Wisthaler, A.: The molecular identification of organic compounds in the atmosphere: state of the art and challenges, Chem. Rev., 115, 3919-3983, 10.1021/cr5003485, 2015.

Ohno, T., He, Z., Sleighter, R. L., Honeycutt, C. W., and Hatcher, P. G.: Ultrahigh resolution mass spectrometry and indicator species analysis to identify marker components of soil- and plant biomass- derived organic matter fractions, Environ. Sci. Technol., 44, 8594-8600, 10.1021/es101089t, 2010.

Painter, T. H., Deems, J. S., Belnap, J., Hamlet, A. F., Landry, C. C., and Udall, B.: Response of Colorado River runoff to dust radiative forcing in snow, Proc. Nat.

Acad. Sci. U.S.A., 107, 17125-17130, 10.1073/pnas.0913139107, 2010.

Painter, T. H., Seidel, F. C., Bryant, A. C., McKenzie Skiles, S., and Rittger, K.: Imaging spectroscopy of albedo and radiative forcing by light-absorbing impurities in mountain snow, J. Geophys. Res. Atmos., 118, 9511-9523, 10.1002/jgrd.50520, 2013.

Pluskal, T., Castillo, S., Villar-Briones, A., and Orešič, M.: MZmine 2: modular framework for processing, visualizing, and analyzing mass spectrometry-based molecular profile data, BMC Bioinf., 11, 395, 10.1186/1471-2105-11-395, 2010.

Pöhlker, C., Huffman, J. A., and Pöschl, U.: Autofluorescence of atmospheric bioaerosols – fluorescent biomolecules and potential interferences, Atmos. Meas. Tech., 5, 37-71, 10.5194/amt-5-37-2012, 2012.

Pu, W., Wang, X., Wei, H. L., Zhou, Y., Shi, J. S., Hu, Z. Y., Jin, H. C., and Chen, Q. L.: Properties of black carbon and other insoluble light-absorbing particles in seasonal snow of northwestern China, The Cryosphere, 11, 1213-1233, 10.5194/tc-11-1213-2017, 2017.

Pu, W., Cui, J., Shi, T., Zhang, X., He, C., and Wang, X.: The remote sensing of radiative forcing by light-absorbing particles (LAPs) in seasonal snow over northeastern China, Atmos. Chem. Phys. , 19, 9949-9968, 10.5194/acp-19-9949-2019, 2019.

Qi, Y., Fu, P., and Volmer, D. A.: Analysis of natural organic matter via fourier transform ion cyclotron resonance mass spectrometry: an overview of recent non-petroleum applications, Mass Spectrom. Rev., 00, 1-15, 10.1002/mas.21634, 2020.

Qian, Y., Wang, H., Zhang, R., Flanner, M. G., and Rasch, P. J.: A sensitivity study on modeling black carbon in snow and its radiative forcing over the Arctic and Northern China, Environ. Res. Lett. , 9, 10.1088/1748-9326/9/6/064001, 2014.

Roach, P. J., Laskin, J., and Laskin, A.: Higher-order mass defect analysis for mass spectra of complex organic mixtures, Anal. Chem., 83, 4924-4929, 10.1021/ac200654j, 2011.

Saleh, R.: From Measurements to Models: Toward Accurate Representation of Brown Carbon in Climate Calculations, Curr. Pollut. Rep., 6, 90-104, 10.1007/s40726-020-00139-3, 2020.

Seinfeld, J. H., and Pandis, S. N.: Atmospheric chemistry and physics: from air pollution to climate change, 3rd ed., John Wiley & Sons, 2016.

Shi, T., Pu, W., Zhou, Y., Cui, J., Zhang, D., and Wang, X.: Albedo of Black Carbon-Contaminated Snow Across Northwestern China and the Validation With Model Simulation, J. Geophys. Res. Atmos., 125, 10.1029/2019jd032065, 2020.

Shick, J. M., and Dunlap, W. C.: Mycosporine-like amino acids and related Gadusols: biosynthesis, acumulation, and UV-protective functions in aquatic organisms, Annu. Rev. Physiol., 64, 223-262, 10.1146/annurev.physiol.64.081501.155802, 2002.

Siegmann, K., and Sattler, K.: Formation mechanism for polycyclic aromatic hydrocarbons in methane flames, J. Chem. Phys., 112, 698-709, 10.1063/1.480648, 2000.

Singer, G. A., Fasching, C., Wilhelm, L., Niggemann, J., Steier, P., Dittmar, T., and Battin, T. J.: Biogeochemically diverse organic matter in Alpine glaciers and its downstream fate, Nat. Geosci., 5, 710-714, 10.1038/NGEO1581, 2012.

Skiles, S. M., Flanner, M., Cook, J. M., Dumont, M., and Painter, T. H.: Radiative forcing by light-absorbing particles in snow, Nat. Clim. Chang., 8, 964-971, 10.1038/s41558-018-0296-5, 2018.

Spencer, R. G. M., Guo, W. D., Raymond, P. A., Dittmar, T., Hood, E., Fellman, J., and Stubbins, A.: Source and biolability of ancient dissolved organic matter in glacier

and lake ecosystems on the Tibetan Plateau, Geochim. Cosmochim. Acta, 142, 64-74, 10.1016/j.gca.2014.08.006, 2014.

Stedmon, C. A., Markager, S., and Bro, R.: Tracing dissolved organic matter in aquatic environments using a new approach to fluorescence spectroscopy, Mar. Chem., 82, 239-254, 10.1016/S0304-4203(03)00072-0, 2003.

Stedmon, C. A., and Markager, S.: Resolving the variability in dissolved organic matter fluorescence in a temperate estuary and its catchment using PARAFAC analysis, Limnol. Oceanogr., 50, 686-697, 10.4319/lo.2005.50.2.0686, 2005.

Stedmon, C. A., and Bro, R.: Characterizing dissolved organic matter fluorescence with parallel factor analysis: a tutorial, Limnol. Oceanogr.-Meth., 6, 572-579, 10.4319/lom.2008.6.572, 2008.

Sun, H. L., Biedermann, L., and Bond, T. C.: Color of brown carbon: A model for ultraviolet and visible light absorption by organic carbon aerosol, Geophys. Res. Lett. , 34, L17813, 10.1029/2007gl029797, 2007.

Toon, O. B., Mckay, C. P., Ackerman, T. P., and Santhanam, K.: Rapid Calculation of Radiative Heating Rates and Photodissociation Rates in Inhomogeneous Multiple-Scattering Atmospheres, J. Geophys. Res. Atmos., 94, 16287-16301, 10.1029/JD094iD13p16287, 1989.

Voisin, D., Jaffrezo, J. L., Houdier, S., Barret, M., Cozic, J., King, M. D., France, J. L., Reay, H. J., Grannas, A., Kos, G., Ariya, P. A., Beine, H. J., and Domine, F.: Carbonaceous species and humic like substances (HULIS) in Arctic snowpack during OASIS field campaign in Barrow, J. Geophys. Res. Atmos., 117, D00r19, 10.1029/2011jd016612, 2012.

Wang, K., Zhang, Y., Huang, R.-J., Cao, J., and Hoffmann, T.: UHPLC-Orbitrap mass spectrometric characterization of organic aerosol from a central European city (Mainz, Germany) and a Chinese megacity (Beijing), Atmos. Environ., 189, 22-29, 10.1016/j.atmosenv.2018.06.036, 2018.

Wang, X., Doherty, S. J., and Huang, J.: Black carbon and other light-absorbing impurities in snow across Northern China, J. Geophys. Res. Atmos., 118, 1471-1492, 10.1029/2012JD018291, 2013.

Wang, X., Hayeck, N., Brüggemann, M., Yao, L., Chen, H., Zhang, C., Emmelin, C., Chen, J., George, C., and Wang, L.: Chemical Characteristics of Organic Aerosols in Shanghai: A Study by Ultrahigh-Performance Liquid Chromatography Coupled With Orbitrap Mass Spectrometry, J. Geophys. Res. Atmos., 122, 11,703-711,722, 10.1002/2017jd026930, 2017a.

Wang, X., Pu, W., Ren, Y., Zhang, X., Zhang, X., Shi, J., Jin, H., Dai, M., and Chen, Q.: Observations and model simulations of snow albedo reduction in seasonal snow due to insoluble light-absorbing particles during 2014 Chinese survey, Atmos. Chem. Phys., 17, 2279-2296, 10.5194/acp-17-2279-2017, 2017b.

Wang, X., Hayeck, N., Brüggemann, M., Abis, L., Riva, M., Lu, Y., Wang, B., Chen, J., George, C., and Wang, L.: Chemical characteristics and brown carbon chromophores of atmospheric organic aerosols over the Yangtze River channel: a cruise campaign, J. Geophys. Res. Atmos., 10.1029/2020jd032497, 2020a.

Wang, X., Zhang, X., and Di, W.: Development of an improved two-sphere integration technique for quantifying black carbon concentrations in the atmosphere and seasonal snow, Atmos. Meas. Tech., 13, 39-52, 10.5194/amt-13-39-2020, 2020b.

Wiscombe, W. J., and Warren, S. G.: A Model for the Spectral Albedo of Snow .1. Pure Snow, J. Atmos. Sci., 37, 2712-2733, 10.1175/1520-0469(1980)037<2712:AMFTSA>2.0.CO;2, 1980.

Wu, C., Yang, J., Fu, Q., Zhu, B., Ruan, T., and Jiang, G.: Molecular characterization

of water-soluble organic compounds in PM2.5 using ultrahigh resolution mass spectrometry, Sci. Total Environ. , 668, 917-924, 10.1016/j.scitotenv.2019.03.031, 2019a.

Wu, G., Ram, K., Fu, P., Wang, W., Zhang, Y., Liu, X., Stone, E. A., Pradhan, B. B., Dangol, P. M., Panday, A. K., Wan, X., Bai, Z., Kang, S., Zhang, Q., and Cong, Z.: Water-Soluble Brown Carbon in Atmospheric Aerosols from Godavari (Nepal), a Regional Representative of South Asia, Environ. Sci. Technol., 53, 3471-3479, 10.1021/acs.est.9b00596, 2019b.

Wu, G., Wan, X., Ram, K., Li, P., Liu, B., Yin, Y., Fu, P., Loewen, M., Gao, S., Kang, S., Kawamura, K., Wang, Y., and Cong, Z.: Light absorption, fluorescence properties and sources of brown carbon aerosols in the Southeast Tibetan Plateau, Environ. Pollut., 257, 113616, 10.1016/j.envpol.2019.113616, 2020.

Wu, G., Fu, P., Ram, K., Song, J., Chen, Q., Kawamura, K., Wan, X., Kang, S., Wang, X., Laskin, A., and Cong, Z.: Fluorescence characteristics of water-soluble organic carbon in atmospheric aerosol, Environ. Pollut., 268, 115906, https://doi.org/10.1016/j.envpol.2020.115906, 2021.

Xie, Q., Su, S., Chen, S., Zhang, Q., Yue, S., Zhao, W., Du, H., Ren, H., Wei, L., dong, c., Xu, Y.-s., Sun, Y., Wang, Z., and Fu, P.: Molecular Characterization of Size-Segregated Organic Aerosols in the Urban Boundary Layer in Wintertime Beijing by FT-ICR MS, Faraday Discuss., 10.1039/d0fd00084a, 2020.

Xu, C., Chen, Y., Yang, Y., Hao, X., and Shen, Y.: Hydrology and water resources variation and its response to regional climate change in Xinjiang, J. Geog. Sci., 20, 599-612, 10.1007/s11442-010-0599-6, 2010.

Yan, F. P., Kang, S. C., Li, C. L., Zhang, Y. L., Qin, X., Li, Y., Zhang, X. P., Hu, Z. F., Chen, P. F., Li, X. F., Qu, B., and Sillanpaa, M.: Concentration, sources and light absorption characteristics of dissolved organic carbon on a medium-sized valley glacier, northern Tibetan Plateau, Cryosphere, 10, 2611-2621, 10.5194/tc-10-2611-2016, 2016.

Yang, W., Han, C., Yang, H., and Xue, X.: Significant HONO formation by the photolysis of nitrates in the presence of humic acids, Environ. Pollut. , 243, 679-686, 10.1016/j.envpol.2018.09.039, 2018.

Ye, H., Zhang, R. D., Shi, J. S., Huang, J. P., Warren, S. G., and Fu, Q.: Black carbon in seasonal snow across northern Xinjiang in northwestern China, Environ. Res. Lett., 7, 044002, 10.1088/1748-9326/7/4/044002, 2012.

Zatko, M. C., Grenfell, T. C., Alexander, B., Doherty, S. J., Thomas, J. L., and Yang, X.: The influence of snow grain size and impurities on the vertical profiles of actinic flux and associated NOx emissions on the Antarctic and Greenland ice sheets, Atmos. Chem. Phys., 13, 3547-3567, 2013.

Zhang, Y., Kang, S., Gao, T., Schmale, J., Liu, Y., Zhang, W., Guo, J., Du, W., Hu, Z., Cui, X., and Sillanpaa, M.: Dissolved organic carbon in snow cover of the Chinese Altai Mountains, Central Asia: Concentrations, sources and light-absorption properties, Sci. Total Environ., 647, 1385-1397, 10.1016/j.scitotenv.2018.07.417, 2019.

Zhang, Y., Kang, S., Gao, T., Sprenger, M., Dou, T., Han, W., Zhang, Q., Sun, S., Du, W., Chen, P., Guo, J., Cui, X., and Sillanpää, M.: Dissolved organic carbon in Alaskan Arctic snow: concentrations, light-absorption properties, and bioavailability, Tellus B, 72, 1-19, 10.1080/16000889.2020.1778968, 2020.

Zhang, Y. L., Zhang, E. L., Yin, Y., van Dijk, M. A., Feng, L. Q., Shi, Z. Q., Liu, M. L., and Qin, B. Q.: Characteristics and sources of chromophoric dissolved organic matter in lakes of the Yungui Plateau, China, differing in trophic state and altitude,

Limnol. Oceanogr., 55, 2645-2659, 10.4319/lo.2010.55.6.2645, 2010.

Zhang, Y. L., El-Haddad, I., Huang, R. J., Ho, K. F., Cao, J. J., Han, Y. M., Zotter, P., Bozzetti, C., Daellenbach, K. R., Slowik, J. G., Salazar, G., Prevot, A. S. H., and Szidat, S.: Large contribution of fossil fuel derived secondary organic carbon to water soluble organic aerosols in winter haze in China, Atmos. Chem. Phys., 18, 4005-4017, 10.5194/acp-18-4005-2018, 2018a.

Zhang, Y. L., Kang, S. C., Sprenger, M., Cong, Z. Y., Gao, T. G., Li, C. L., Tao, S., Li, X. F., Zhong, X. Y., Xu, M., Meng, W. J., Neupane, B., Qin, X., and Sillanpaa, M.: Black carbon and mineral dust in snow cover on the Tibetan Plateau, The Cryosphere, 12, 413-431, 10.5194/tc-12-413-2018, 2018b.

Zhao, C., Hu, Z., Qian, Y., Leung, L. R., Huang, J., Huang, M., Jin, J., Flanner, M. G., Zhang, R., Wang, H., Yan, H., Lu, Z., and Streets, D. G.: Simulating black carbon and dust and their radiative forcing in seasonal snow: a case study over North China with field campaign measurements, Atmos. Chem. Phys., 14, 11475-11491, 10.5194/acp-14-11475-2014, 2014.

Zhao, Y., Song, K., Wen, Z., Li, L., Zang, S., Shao, T., Li, S., and Du, J.: Seasonal characterization of CDOM for lakes in semiarid regions of Northeast China using excitation–emission matrix fluorescence and parallel factor analysis (EEM–PARAFAC), Biogeosciences, 13, 1635-1645, 10.5194/bg-13-1635-2016, 2016.

Zhou, L., Zhou, Y., Hu, Y., Cai, J., Liu, X., Bai, C., Tang, X., Zhang, Y., Jang, K. S., Spencer, R. G. M., and Jeppesen, E.: Microbial production and consumption of dissolved organic matter in glacial ecosystems on the Tibetan Plateau, Water Res., 160, 18-28, 10.1016/j.watres.2019.05.048, 2019a.

Zhou, Y., Wen, H., Liu, J., Pu, W., Chen, Q., and Wang, X.: The optical characteristics and sources of chromophoric dissolved organic matter (CDOM) in seasonal snow of northwestern China, The Cryosphere, 13, 157-175, 10.5194/tc-13-157-2019, 2019b.

Zhou, Y., Zhou, L., He, X., Jang, K. S., Yao, X., Hu, Y., Zhang, Y., Li, X., Spencer, R. G. M., Brookes, J. D., and Jeppesen, E.: Variability in Dissolved Organic Matter Composition and Biolability across Gradients of Glacial Coverage and Distance from Glacial Terminus on the Tibetan Plateau, Environ. Sci. Technol., 53, 12207-12217, 10.1021/acs.est.9b03348, 2019c.